Focal mechanisms of earthquake multiplets in the western part of the Corinth Rift (Greece): influence of the velocity model and constraints on the geometry of the active faults

M. Godano, Anne Deschamps, Sophie Lambotte, H. Lyon-Caen, Pascal Bernard, F. Pacchiani

Geophysical Journal International

Geophys. J. Int. (2014) **197,** 1660–1680
Advance Access publication 2014 March 13

doi: 10.1093/gji/ggu059

Focal mechanisms of earthquake multiplets in the western part of the Corinth Rift (Greece): influence of the velocity model and constraints on the geometry of the active faults

Maxime Godano,[1,2] Anne Deschamps,[1] Sophie Lambotte,[3] Hélène Lyon-Caen,[4] Pascal Bernard[2] and Francesco Pacchiani[4,5]

[1] *Géoazur, Université de Nice Sophia Antipolis - CNRS - IRD - OCA, Valbonne-Sophia Antipolis, France. E-mail: godano@ipgp.fr*
[2] *Institut de Physique du Globe de Paris, Sorbonne Paris Cité, Univ. Paris Diderot, UMR*7154 *CNRS, Paris, France*
[3] *Institut de Physique du Globe de Strasbourg, ULP-CNRS, EOST, Strasbourg, France*
[4] *Laboratoire de Géologie, Ecole Normale Supérieure – CNRS, Paris, France*
[5] *WAPMERR, Geneva, Switzerland*

Accepted 2014 February 14. Received 2014 February 14; in original form 2013 July 31

SUMMARY

The composite fault plane solutions for 24 large multiplets recorded in the western part of the Corinth Rift between 2000 and 2007 are computed by jointly inverting *P* polarities and *Sv*/*P*, *Sh*/*P*, *Sv*/*Sh* amplitude ratios of the direct waves. The fault plane solutions are determined using 1-D and 3-D velocity models. Solutions computed with the 3-D velocity model are preferred to the ones computed with the 1-D model because overall, 3-D solutions have a better score function. They correspond essentially to E–NE/W–SW and W–NW/E–SE striking normal faults, which is consistent with the N–S extensional/vertical shortening tectonic regime of the area. For 15 multiplets, one of the nodal planes is similar to the plane delineated by the earthquakes. It is then possible to determine which nodal plane is the fault plane. The analysis of the fault plane solutions highlights a clear decrease of their dip with depth and towards the north. Several multiplets with steeply dipping fault planes (50°–60°) located at depths of 7–8 km are clearly located at the base of onshore and offshore faults that crop out close to the south border of the Corinth Gulf, indicating that these faults are steep down to 7–8 km depth. To the north, multiplets underline a low angle north-dipping structure (20°–30°) on which steep north-dipping faults could take root.

Key words: Earthquake source observations; Seismicity and tectonics; Continental tectonics: extensional; Dynamics: seismotectonics; Fractures and faults.

GJI Seismology

1 INTRODUCTION

Long-term observations (since early 1990s) of the crustal deformation in the Corinth Rift area show some main features. The extension rate across the Gulf measured by repeated GPS campaigns, decreases from 1.5 cm yr^{-1} in the western part to 1.0 cm yr^{-1} in the eastern part (e.g. Avallone *et al.* 2004). The almost NS extension is associated with EW asymmetric active crustal structures and uplifted Neogene terraces on the southern border of the Corinth Gulf (e.g. Armijo *et al.* 1996; Ford *et al.*, in preparation). Active normal faults have been mapped on both sides of the Gulf; the density and the length of these faults are largest on the western southern border area. Little is known on the south dipping faults, which affect the northern border of the Rift. Observed faults which cut the terraces onland in northern Peloponnesus are better documented. The northward dipping faults become younger going northwards and the most recent ones are likely offshore, even though little is known on the fault distribution offshore in the Gulf.

Historical and instrumental large earthquakes over the two last centuries evidence an east–west variation. On the eastern side, the 1981 Corinth sequence of three $M \geq 6$ events has been described as breaking onshore and offshore faults dipping north and south (King *et al.* 1985). On the western side, two different kinds of events have been described (Ambraseys & Jackson 1990; Briole *et al.* 1993; Bernard *et al.* 1997; Papazachos & Papazachou 1997): (1) intermediate magnitude events ($5.8 < M < 6.5$) with hypocentres below the northern coast at depth of about 10 km with no evidence of surface rupture (e.g. 1965 offshore Itea city, 1970 offshore Antikyra city, 1992 offshore Galaxidi city, 1995 Aigion event) and (2) larger events rupturing the surface on the southern coast (e.g. Helike event in 1861 associated with the large Helike north dipping fault). Most of the main events of the last 30 yr correspond to normal faulting events on approximately EW-oriented faults (Fig. 1). Some focal solutions of smaller events (Appendix A) can exhibit some strike-slip component (Pacchiani 2006).

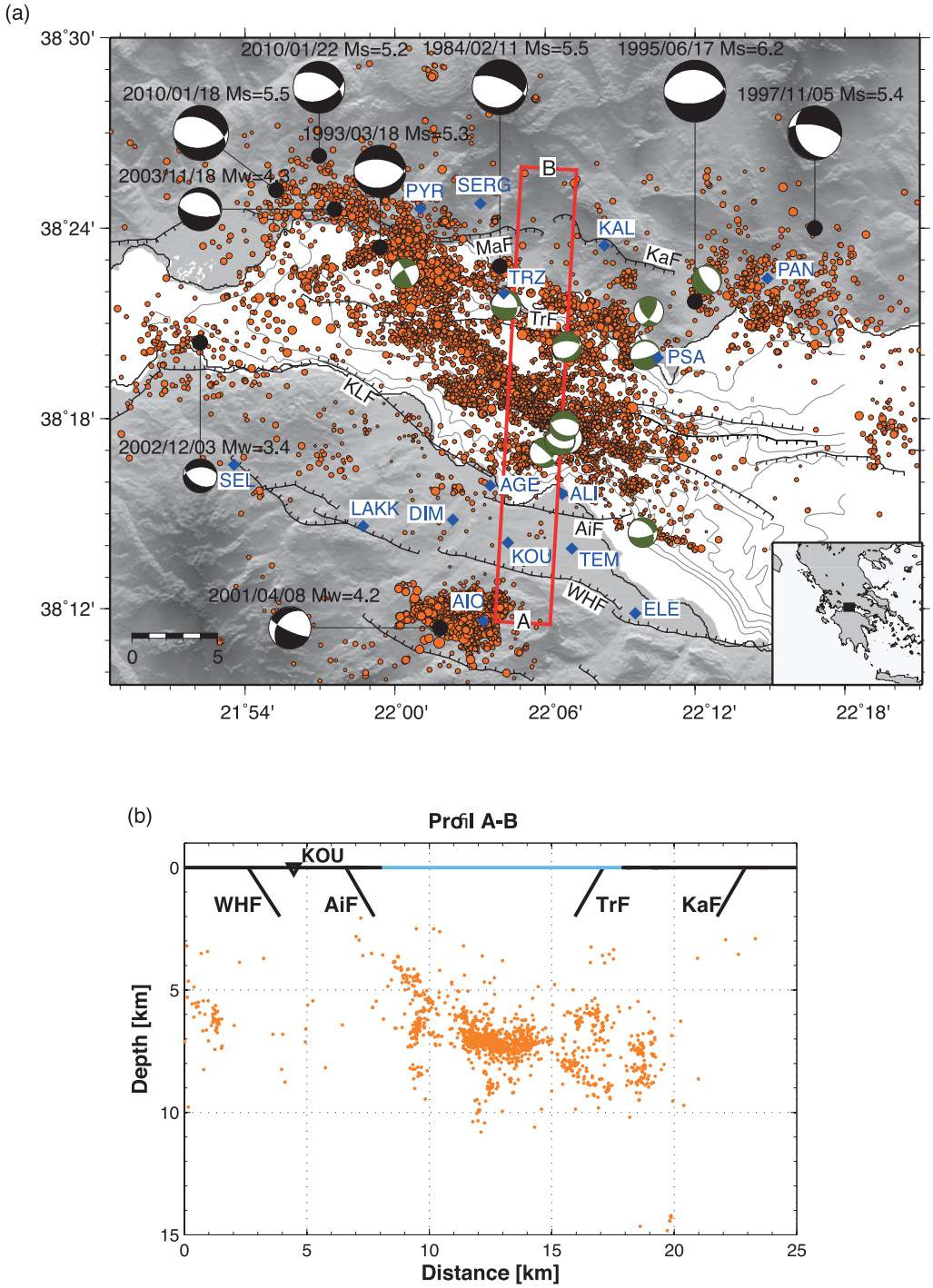

Figure 1. (a) Map of the seismicity between 2001 and 2007 in the Western part of the Corinth Rift recorded by the CRL network (blue squares) and relocated by Lambotte *et al.* (in preparation). Focal mechanisms of the large earthquakes (black) are from Bernard *et al.* (1997), Sokos *et al.* (2012) and Harvard CMT. Focal mechanisms of the microseismicity (green) are from Pacchiani (2006). The fault traces are the main features compiled and presented in Ford *et al.* (in preparation) based on Moretti *et al.* (2003), Palyvos *et al.* 2005 and original field work. WHF, West Helike Fault; AiF, Aigion Fault; KLF, Kamarai and Lambiri fault system; TrF, Trizonia Fault; KaF, Kalithea Fault; MaF, Marathia Fault. (b) N–S cross-section (modified from Lambotte *et al.*, in preparation).

The microseismicity is mainly concentrated below the Gulf and is clearly inhomogeneous along the Corinth Rift: the seismic activity is very intense in the western area and stops abruptly at the transition zone, between the narrow shallow western rift and the broader, deeper eastern rift around longitude 22.2° (Bernard *et al.* 2006; Lambotte *et al.*, in preparation; Fig. 1).

Two different temporary seismicity experiments have been used to infer the velocity structure in the region. In 1991, a 2-month deployment of 51 seismological stations allowed Rigo *et al.* (1996) to produce a mean 1-D model, which is extensively used for events location over the western part of the Corinth Rift. In 2002 a 6-month experiment covering the same area (deployment of 49

three-component stations on the southern and northern coasts completed by three three-component ocean bottom seismometers deployed during 1 month in the centre of the Gulf) produced a new data set. Compared with the 1991 data set, the 2002 data set is improved thanks to a better covering and instrumental homogeneity. Traveltime tomography using asymptotic ray theory and finite frequency ray theory has provided 3-D V_p and V_s models (Gautier *et al.* 2006, 2008).

In 2000/2001 a permanent dense seismic network of 12 short-period three-component stations, the Corinth Rift Laboratory Network (CRLNET, Lyon-Caen *et al.* 2004), was installed around Aigion area on both sides of the Corinth Rift. This network, completed with data provided by Athens University (LAKK), Patras University (SEL) and Prague University (SERG), allows to follow with a good precision the western rift seismic activity.

A detailed study of the 2000–2007 microseismicity consisting in (1) identification of multiplets and (2) relocation of the whole seismicity using a double difference technique (Waldhauser & Ellsworth 2000) was performed by Lambotte *et al.* (in preparation). Events were classified in multiplets by evaluating waveform similarity. This was done by computing cross-correlations between earthquakes and the reference event of each multiplet already identified as well as events not classified in multiplets. Relocation was performed with HYPODD software in an LSQR (least squares) mode. The 1-D velocity model used is from Rigo *et al.* (1996). Double differences from both absolute time catalogue and cross-correlation from multiplets were integrated. The relative locations are well constrained in the centre of the rift (maximal errors of the order of 30 m) where there is a high density of events and are less well constrained to the west where the network coverage is not optimum with respect to the seismicity (maximal errors of the order of 200–300 m). Seismicity relocation shows that the activity is distributed on different crustal structures. Schematically, the following must be considered (1) a large active zone beneath the Gulf of Corinth dipping north at low angle (∼20°) from 7–8 km below the southern coast to 11–12 km below the northern one, on which large events like the 1995 Aigion event have occurred and (2) a shallower crustal activity mainly above this zone (but some seismic activity is nevertheless observed below this zone) and structured in swarms (Fig. 1); the spatial distribution of these swarms seems to indicate the presence of high angle (50°–60°) north dipping crustal structures located at the downward extension of faults mapped on the southern coast. The better known structure is the Aigion Fault, which has been cut by a drilling at 750 m, confirming a 50°–60° dip towards north. The activated structures may stop or not on the main low angle deeper structure.

In this paper, we focus on the determination of focal solutions and associated uncertainties for the multiplets presented in Lambotte *et al.* (in preparation). The fault plane parameters are an independent estimation of the geometry of the active structures at depth, and Rietbrock *et al.* (1996) have shown that associating fault plane solutions with multiplet geometry allows to characterize the deformation associated with a multiplet. In a first part, we present the methodology used to compute focal mechanisms which is based on the joint inversion of *P* polarities and *Sv*/*P*, *Sh*/*P*, *Sv*/*Sh* amplitude ratios of the direct waves. Due to the limited number of stations which were able to record these small events with a sufficient high signal-to-noise ratio and the very good similarity of waveforms, we propose a composite analysis (determination of one focal mechanism from polarities and amplitude ratios of several earthquakes). We also assess the influence of the velocity model (1-D versus 3-D) on the focal solution determination. In a second part, we compare the fault plane solutions with the geometrical parameters of the multiplets.

2 METHODOLOGY

2.1 Focal mechanism in 1-D velocity model

The fault plane solutions are computed by jointly inverting the polarities of the direct *P* waves and the amplitude ratios between the direct *P*, *Sv* and *Sh* waves (*Sv*/*P*, *Sh*/*P*, *Sv*/*Sh*). The amplitudes constrain better the solution than the *P* polarities alone. However, they are subject to distortion caused by structural heterogeneities along the seismic wave path. The effect of the distortion can be reduced by using amplitude ratios for focal mechanism determination (e.g. Julian *et al.* 1998).

The amplitude is defined as the peak of the first half-cycle of the direct wave (*P* or *S*). Practically, the *P* polarity and amplitude are manually measured on the vertical (*Z*) component of a velocigram. The horizontal components are rotated into the radial (R) and transverse (T) components. The *Sv* and *Sh* amplitudes are manually measured on the R and T component, respectively (Fig. 2). The amplitudes are measured on [1 Hz; 5 Hz] Butterworth bandpass filtered seismograms. This filter is suitable for removing the high-frequency noise affecting the waveforms (see Appendix B). The observed amplitudes (measured in counts on the velocigrams) are next converted in velocity by removing the gain and the instrumental response.

The focal mechanisms are determined using the non-linear inversion method of the direct *P*, *Sv* and *Sh* amplitudes developed by Godano *et al.* (2009). We modify this method for taking into account the amplitude ratios. In practice we use the direct problem described in Godano *et al.* (2009) and summarized hereinafter to first compute theoretical *P*, *Sv* and *Sh* amplitude for a point source in the flat layered medium of Rigo *et al.* (1996) and next take amplitude ratios. Following ray theory (e.g. Aki & Richards 1980), the elastic far-field displacement of a direct seismic phase *k* (*P*, *Sv* or *Sh*) in an inhomogeneous and isotropic medium is given by:

$$u(t) = \left(\frac{M_0}{4\pi \sqrt{\rho_0 \rho_s c_0 c_s c_0^2 R^k}} F^k \prod \left(L_j^k\right) C \Delta \dot{s}(t - T^k) \right) \times a(t), \tag{1}$$

where M_0 is the scalar moment, ρ_0 is the density at the source, ρ_s is the density at the station, c_0 is the velocity of the phase *k* at the source, c_s is the velocity of the phase *k* at the station, R^k is the geometrical spreading of the phase *k*, L_j^k is the transmission coefficient at the *j*-th interface along the ray path of the phase k, *C* is a correction coefficient if the station is at the free surface, and T^k is the source–station time propagation of the phase k. $\Delta \dot{s}(t - T^k)$ is the source time function expression set as a triangular function. $F^k(\phi, i, \phi_f, \delta, \lambda)$ is the expression of the radiation coefficient of the phase *k* where ϕ is the azimuth of the ray at the source, *i* is the ray take-off angle at the source, ϕ_f is the azimuth of the fault plane, δ is the dip of the fault plane and λ is the rake of the fault plane. The modelling also includes the anelastic attenuation of the medium $a(t)$. We take a quality factor *Q* of 350 for *P* and *S* waves (value estimated for the upper 20 km of the crust in Greece, Papazachos 1992). The theoretical amplitudes are automatically measured on synthetic velocigrams which are obtained by taking the temporal derivative of the far-field displacement.

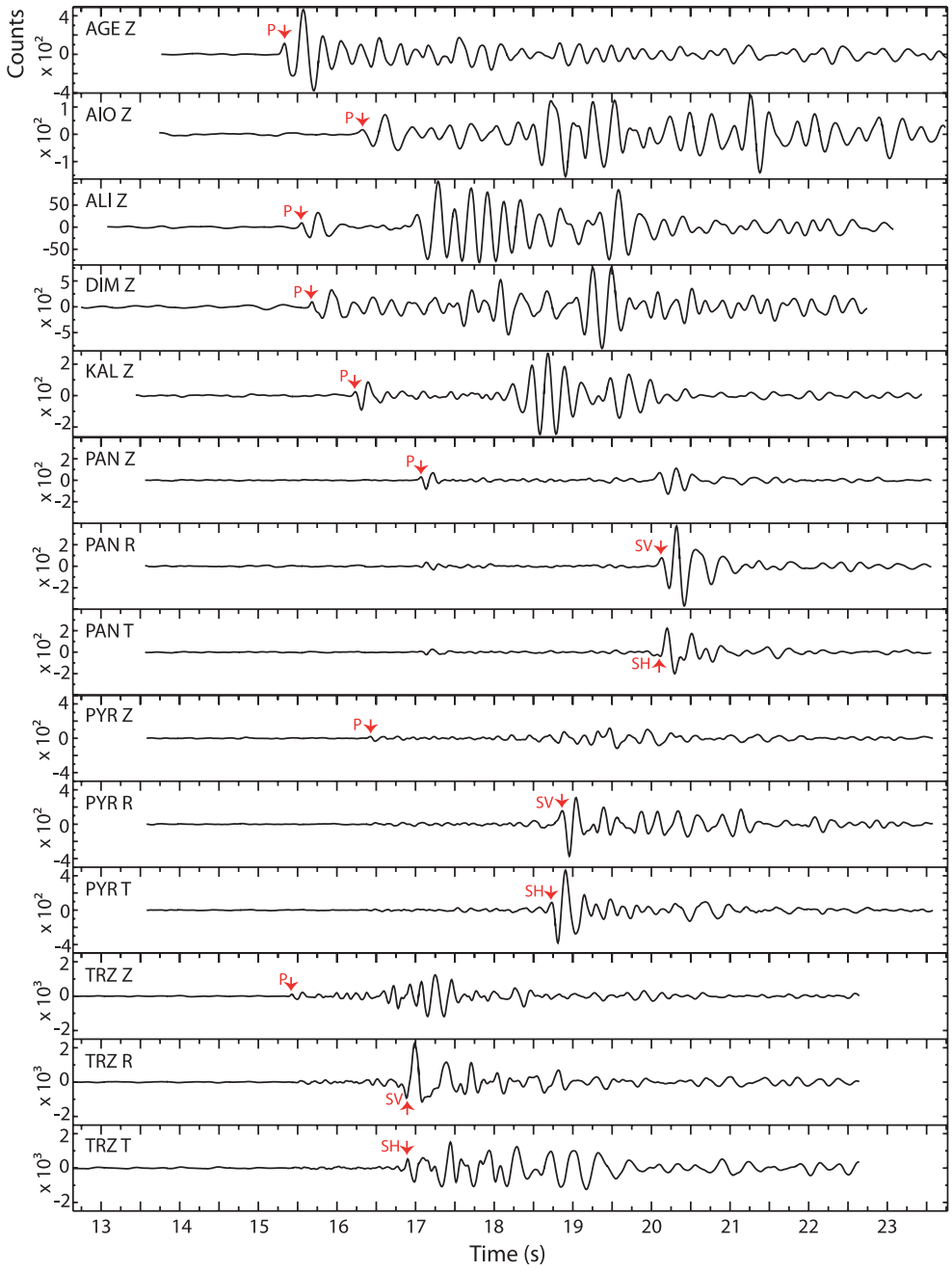

Figure 2. Examples of Butterworth bandpass filtered 1–5 Hz velocity records for the 2004 January 29 01:25:34 earthquake (multiplet 04432). For the stations AGE, AIO, ALI, DIM and KAL only the vertical component is represented because at these stations, only the *P* wave (measured on the vertical component) is used in the inversion. For the stations PAN, PYR and TRZ, the horizontal traces have been rotated into the radial and tranverse components. The *P*, *Sv* and *Sh* amplitudes used for the fault plane solution determination are indicated by the red vertical arrows.

The inverse problem is solved by random exploration through a simulated annealing algorithm (Kirkpatrick *et al.* 1983). The parameter values explored are ϕ_f, δ and λ. At each step j, two score functions are computed. The first measures the fit between the calculated and the observed amplitude ratios:

$$S_j^{\text{ratio}} = \exp\left(-\frac{1}{N}\sum_{i=1}^{N}\left|\log_{10}\left(d_i^{\text{obs}}\right) - \log_{10}\left(d_i^{\text{calc}}\right)\right|\right), \quad (2)$$

where N is the number of amplitude ratios, d_i^{obs} is the i-th observed amplitude ratio and d_i^{calc} is the i-th calculated amplitude ratio. The use of the base 10 logarithm of the amplitude ratio is more stable than using simple amplitude ratios (e.g. Snoke *et al.* 1984; Jechumtalova & Šileny 2005). The second score function is dependent on the number of opposition (n) between the observed and calculated *P* polarities:

$$S_j^{\text{pol}} = \exp(-0.5n). \quad (3)$$

The global score function associated to the explored solution j is given by:

$$S_j^G = S_j^{\text{ratio}}.S_j^{\text{pol}}. \quad (4)$$

The exploration is divided in three steps. The first one enables a wide exploration of the space parameters to localize areas of

high score. The second one converges towards the area of absolute maximum score but can get out to explore other areas. Details of these two steps are described in Godano *et al.* (2009). In this study, we added a third step consisting in a fine exploration of the area of absolute maximum score to ensure that the optimal solution is precisely found.

The *P* polarity is a strong piece of information that allows determining the compressional and dilatational zones on the focal sphere. Hence, the score function is designed for allowing a preferential exploration of the solutions giving *P* polarities in accordance with the observations. For solutions without *P* polarity contradiction, $S^{\mathrm{G}} = S^{\mathrm{ratio}}$. In case of one polarity contradiction, S^{G} decreases by 39 per cent, for two contradictions S^{G} decreases by 63 per cent, for three contradictions S^{G} decreases by 78 per cent and so on. Therefore, the optimal solution is the solution best fitting the observed amplitudes ratio among all the explored solutions satisfying the observed *P* polarities. Such a design of the score function (priority to the polarity with respect to the amplitude ratio) requires confidence in the *P* polarity determination. Consequently, we have to be sure that there is no sensor problem giving polarity inversion.

The uncertainties on the focal mechanisms are calculated by accounting for the amplitude picking uncertainties caused by the noise level and the event location uncertainties. Uncertainties on the focal mechanism are computed by performing 100 inversions using random perturbed amplitudes and event locations. The results of these 100 inversions are called 'perturbed solutions'. The measured amplitude is affected by the signal-to-noise ratio. As a consequence, the lower the signal-to-noise ratio, the more the amplitude is modified by the noise. Therefore, in the uncertainties estimation process, the amplitudes are perturbed in increments following a Gaussian distribution with a standard deviation corresponding to that of a noise window immediately before the *P*, *Sv* and *Sh* amplitudes. Hence higher is the noise amplitude, greater is the standard deviation of the noise window and greater is the perturbation applied to amplitudes. The location is perturbed following Gaussian distributions with standard deviations equal to the absolute uncertainties of the event coordinates. Lambotte *et al.* (in preparation) estimate the relative uncertainties (i.e. the earthquake location errors inside the multiplets) but does not evaluate the errors on the multiplet location (absolute uncertainties). Lyon-Caen *et al.* (2004) estimate that errors on absolute locations are less than 1 km in all directions for events inside the network. Nevertheless, we take into account that earthquakes are generally poorer located in depth than in horizontal direction. Therefore, we evaluate the error on absolute location being typically of 500 m in offset and 1000 m in depth.

The distribution of the strike, dip and rake of the 100 perturbed solutions gives the uncertainties $\Delta_{\phi f}$, $\Delta\delta$ and $\Delta\lambda$ for each nodal plane of the optimal solution. These uncertainties are taken as the values delimiting the two-sigma confidence intervals containing 95 per cent of the strike, dip and rake of the perturbed solutions. From these uncertainties, a global confidence interval around the optimal solution can be defined as:

$$I_c = \left[\phi_f^{\mathrm{opt}} - \Delta_{\phi f}, \phi_f^{\mathrm{opt}} + \Delta_{\phi f}\right] \cap \left[\delta^{\mathrm{opt}} - \Delta_\delta, \delta^{\mathrm{opt}} + \Delta_\delta\right] \cap \left[\lambda^{\mathrm{opt}} - \Delta_\lambda, \lambda^{\mathrm{opt}} + \Delta_\lambda\right]. \quad (5)$$

2.2 Focal mechanism in 3-D velocity model

Focal mechanisms are frequently computed using flat layered velocity model (1-D), because a more precise model like a 3-D velocity model is not available. However, when a 3-D model has been determined, it would be better to compute focal mechanisms using it. The take-off angle and azimuth of the ray at the source are dependent of source and station location and velocity model. Hence for a given source and station location, the position of the station on the focal sphere can significantly change for take-off angle and azimuth computed in a 1-D or in a 3-D velocity model. These variations can have a strong influence on the focal mechanism determination since the geometry of the nodal planes is mainly controlled by the position of the stations on the focal sphere.

The direct problem of the method we describe above takes into account only flat layered velocity model. For a more complex velocity model, seismogram modelling in 3-D media would be required. Nevertheless such procedure using modelling methods as finite difference (e.g. Saenger *et al.* 2000) or spectral elements (e.g. Komatitsch *et al.* 2004) are time consuming and require great computational resources.

We avoid these drawbacks by using the following alternative procedure:

(1) Ray take-off angle and azimuth at the source are critical parameters controlling the accuracy of the focal mechanism determination. Therefore, *P* and *S* radiation coefficients (F^k in eq. 1) are precisely determined by calculating take-off angle and azimuth in the 3-D velocity medium of Gautier *et al.* (2006) (this model provides both *P*- and *S*-wave velocity contrary to the 2008 model that provides only *P*-wave velocity). In practice, take-off angle and azimuth are computed with the NonLinLoc software suite (Lomax *et al.* 2000) that uses the eikonal finite-difference scheme (Podvin & Lecomte 1991).

(2) The terms characterizing the propagation medium in eq. (1) are computed using the 1-D velocity model of Rigo *et al.* (1996). This approximation of the 3-D velocity model by the 1-D velocity model seems valid to us because the 3-D velocity model is not far from a layered model. No large lateral variations are exhibited even if some $V_{\mathrm{p}}/V_{\mathrm{s}}$ anomalies are present (Gautier *et al.* 2006). Moreover, as mentioned in Section 2.1 the use of amplitude ratios in the focal mechanism determination procedure tends to attenuate the propagation effects and consequently the effects of the above approximation.

3 COMPOSITE FOCAL MECHANISMS DETERMINATION

In this study, we focus on multiplet earthquakes that are characterized by close hypocentres, very similar waveform and consequently very similar focal mechanisms. An example showing how similar are the waveforms inside a multiplet is displayed in Appendix B. Based on this similarity, we decided to merge the data (*P* polarities and amplitude ratios) of several earthquakes of a multiplet for determining a composite focal mechanism. Considered individually, each earthquake does not necessarily have enough measured polarities and amplitude ratios to compute an accurate fault plane solution. Such composite solution is better constrained than an individual focal mechanism. In practice, we only use the earthquakes with $M_{\mathrm{w}} \geq 1.7$. For the others, the signal-to-noise ratio is poor and prevents to correctly measure the amplitudes.

In the following, the amplitude ratios are only used for the stations of the northern coast of the Corinth Gulf that are deployed at the free surface (KAL, KOU, PAN, PYR, TRI, TRZ). At the other stations, the sensors are deployed in wells and have not been oriented. Hence, it is not possible to rotate the seismogram into the radial and transverse component and measure *Sv* and *Sh* amplitude for these stations.

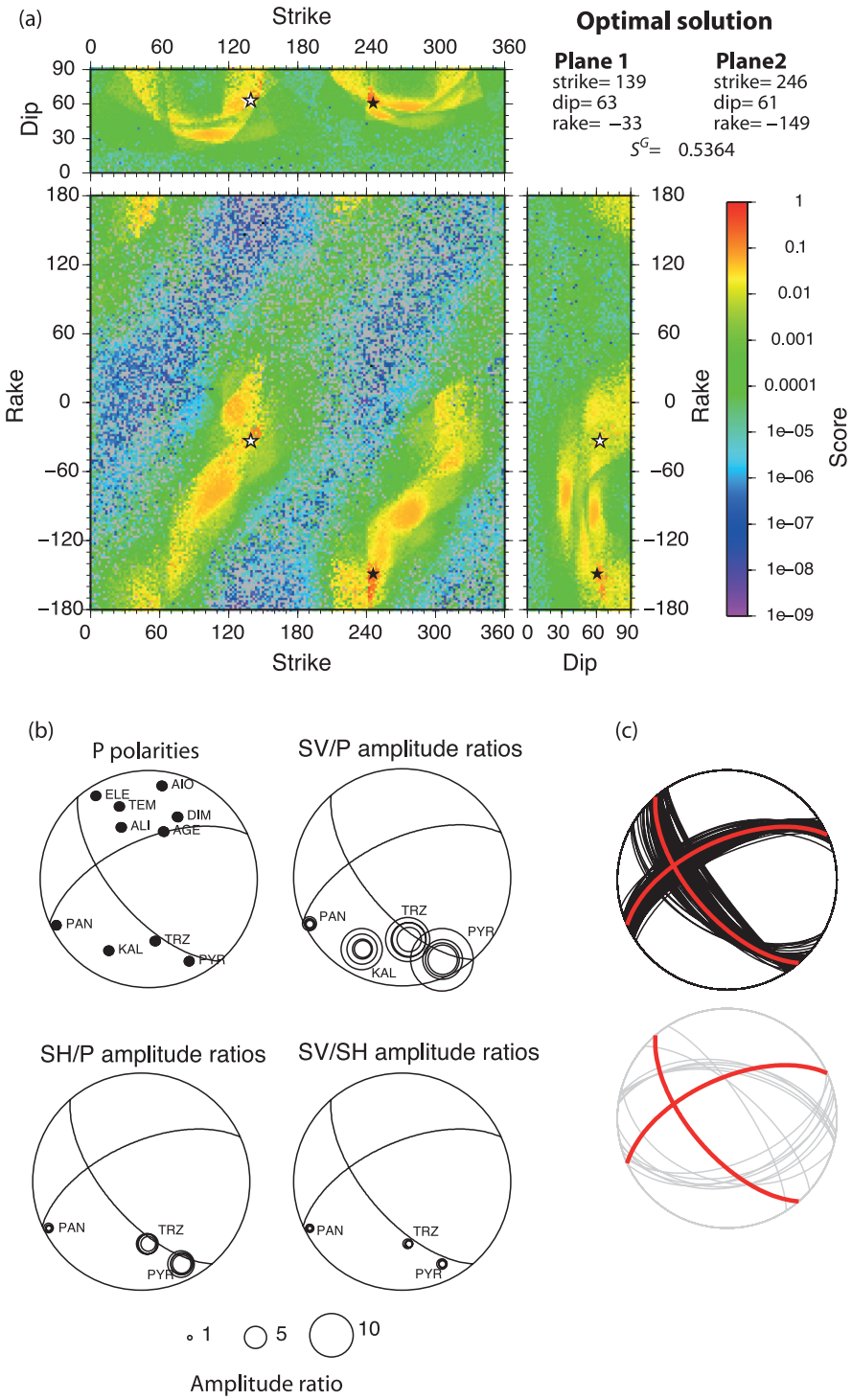

Figure 3. Example of composite focal mechanism determination by jointly inverting *P*-wave polarities and *Sv*/*P*, *Sh*/*P* and *Sv*/*Sh* amplitude ratios for five seismic events of multiplet 04432 and using the 1-D velocity model of Rigo *et al.* (1996). (a) Space of the explored solutions with the associated score after 100 000 iterations. The black and white stars indicate the nodal planes strike, dip and rake of the optimal solution (i.e. solution with highest score). (b) Optimal fault plane solution with the projection of the *P* polarities and amplitude ratios *Sv*/*P*, *Sh*/*P* and *Sv*/*Sh* on the focal sphere. (c) Optimal fault plane solution (red) with its uncertainty domain defined by perturbed solutions inside the confidence interval (eq. 5; black) and outside the confidence interval (grey).

3.1 Example of composite focal mechanism

Fig. 3 gives an example of composite focal mechanism determination (multiplet 04432) using the 1-D velocity model of Rigo *et al.* (1996) (1-D solution). This multiplet is a good example in terms of available *P* polarities (43) and amplitude ratios (40; see Table 1). The space of solutions after 100 000 iterations is displayed in Fig. 3(a). Each explored solution is associated with a score. The exploration has converged towards the optimal solution (normal fault with strike-slip component) associated with the highest score ($S^G = 0.5364$). This optimal solution corresponds to one of the two *P* nodal planes of the optimal focal mechanism (black star,

Table 1. List of the studied multiplets, E–W, N–S, depth coordinates of the multiplet centroid (from a reference point located at 21.6°E and 38°N), number of earthquakes in each multiplet and number of earthquakes, *P* polarities and amplitude ratios used to compute composite focal mechanisms.

Multiplet	*X* (m)	*Y* (m)	*Z* (m)	Number of events in the multiplet	Number of events used for the inversion	*P* polarities	*Sv*/*P* ratios	*Sv*/*Sh* ratios	*Sh*/*P* ratios
00019	46163.99	39874.06	8325.00	40	5	21	5	5	5
00573	52618.95	40768.38	10146.00	18	2	14	3	3	3
00630	48877.43	34080.93	7038.50	11	2	15	3	2	3
00724	44124.33	37523.34	8004.00	20	4	32	6	6	8
00853	40212.50	44667.77	8809.25	21	4	22	7	6	8
00866	47903.45	37436.66	8042.60	58	5	32	9	8	8
00891	48516.72	33919.32	6733.00	13	3	21	7	5	6
01767	56092.88	39994.34	9978.40	11	5	31	10	10	12
02423	53593.72	41711.71	11047.33	49	3	23	9	6	6
02877	41118.75	39733.99	8243.00	39	6	47	8	7	14
03061	37968.09	41139.80	8077.50	15	2	14	6	4	5
03715	55141.02	41679.53	10214.00	27	4	24	13	13	13
03803	39642.43	37682.52	7730.00	15	3	24	2	1	5
03911	43221.83	33225.75	7499.50	30	4	39	12	11	13
03917	44828.16	32623.67	6539.20	21	5	43	1	1	1
04049	48347.86	41914.33	9270.00	15	3	21	10	7	7
04416	42055.15	34326.78	7223.17	23	6	56	20	13	16
04432	41686.05	34423.27	7201.80	19	5	43	16	12	12
04493	41976.91	34243.57	7671.67	15	3	22	5	1	4
04572	40131.94	33982.57	7677.25	19	4	35	4	3	5
04693	42254.77	31759.18	5755.50	15	4	31	6	5	6
04761	38770.69	34648.41	7550.00	17	4	29	6	4	5
05278	42986.69	34658.64	7837.00	26	5	44	10	7	13
18445	40597.89	37017.55	6480.33	15	3	16	9	6	6

$\phi_{f2} = 246°$, $\delta_2 = 61°$, $\lambda_2 = -149°$). The other nodal plane is indicated by the white star ($\phi_{f1} = 139°$, $\delta_1 = 63°$, $\lambda_1 = -33°$).

Fig. 3(b) shows *P* polarities, *Sv*/*P*, *Sh*/*P* and *Sv*/*Sh* amplitude ratio projections on the focal sphere. The optimal focal mechanism is in accordance with the observed *P* polarity of all the stations. As expected, *Sv*/*P* and *Sh*/*P* amplitude ratios are relatively low at stations near the middle of the compressional quadrant (KAL) and are relatively large near the *P* nodal planes (TRZ and PYR). An exception is the station PAN that is nodal and displays relatively low *Sv*/*P* and *Sh*/*P* ratios.

We can observe significant amplitude ratio variations at a single station. These variations are a factor of 2 at stations KAL, PYR and TRZ for the *Sv*/*P* ratio. The amplitude ratios at a given station should be similar since the events constituting a multiplet have similar waveforms. The events are in fact not exactly collocated and the focal mechanisms are not exactly identical. These small differences and errors in the velocity model involve variations in take-off angle and amplitude ratios. Nevertheless, Hardebeck & Shearer (2003) state that these phenomena do not explain the large amplitude ratio variations. The authors invoke other mechanisms as focusing and defocusing effects caused by small-scale velocity heterogeneities producing large amplitude differences for closely spaced events, or scattering of high-frequency energy at the near-surface.

Fig. 3(c) gives the optimal focal mechanism (red) with its associated uncertainty domain. Black solutions correspond to the 'perturbed solutions' inside the confidence interval (eq. 5), grey solutions are the 'perturbed solutions' outside the confidence interval. The uncertainty on the strike, dip and rake are (20°, 10°, 46°) for plane 1 and (34°, 20°, 42°) for plane 2.

The results of the inversion using a 3-D velocity model (3-D solution) are displayed in Fig. 4. The distribution of the stations on the focal sphere is modified, which allows the determination of a fault plane solution different from the one computed with the 1-D velocity model. The optimal solution corresponds to a normal fault ($\phi_{f1} = 85°$, $\delta_1 = 39°$, $\lambda_1 = -100°$ and $\phi_{f2} = 278°$, $\delta_2 = 51°$, $\lambda_2 = -82°$). The corresponding score function ($S^G = 0.6380$) is clearly greater than the score function of the preceding solution. This means that the amplitude ratios are better modelled using the 3-D velocity model. Stations near the middle of the compressional quadrant (PAN and KAL) have relatively low *Sv*/*P* and *Sh*/*P* ratios compared to the nodal station TRZ. However, PYR that is not nodal displays a relatively high ratio.

The uncertainties on the optimal solution are (32°, 23°, 50°) and (32°, 14°, 42°) for the strike, dip and rake of the nodal planes 1 and 2, respectively. The perturbed solutions are distributed following two fault plane families. A main family corresponds to the optimal solution (black in Fig. 4c) and a secondary family (grey) corresponds to the optimal solution of the 1-D inversion. Similarly, a secondary family of solution appears in the 1-D inversion (grey in Fig. 3c) and corresponds to the optimal solution of the 3-D model.

3.2 Application to 24 multiplets

The composite focal mechanisms are computed in 1-D and 3-D velocity models for 24 earthquake multiplets among the biggest multiplets determined by Lambotte *et al.* (in preparation). Table 1 gives the number of earthquakes in each multiplet and the number of earthquakes, *P* polarities and amplitude ratios used to compute the composite focal mechanisms. The list of earthquakes used for the focal solution computation is given in Appendix C. Table 2 gives the 1-D and 3-D fault plane solutions parameters with uncertainties on the strike dip and rake. The 1-D and 3-D optimal focal mechanisms with the perturbed solutions and the projection of the *P* polarities are given in Appendix D. The difference between the

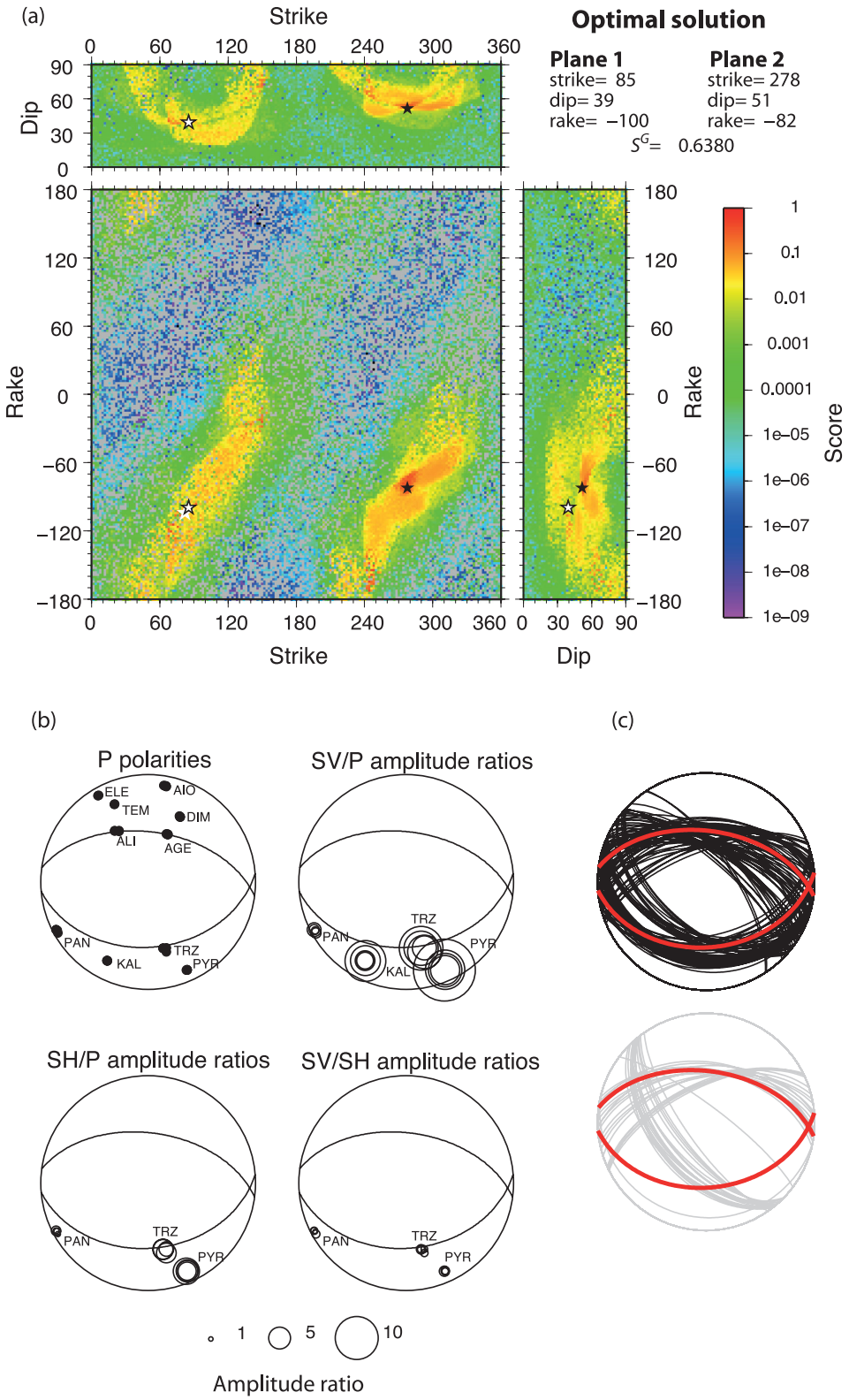

Figure 4. Same as Fig. 3 but for the 3-D velocity model of Gautier *et al.* (2006).

1-D and 3-D fault plane solutions depends on the multiplet. Several multiplets are characterized by solutions significantly different (00019, 00724, 00866, 03911, 03917, 04432, 04493, 04693 and 18445). The variations between the 1-D and 3-D solutions show how the focal mechanism resolution is sensitive to the used velocity models. For most of the multiplets displaying strong variability between 1-D and 3-D focal mechanisms, the optimal 1-D solution is present in perturbed 3-D solutions and inversely, the optimal 3-D solution is present in perturbed 1-D solutions. This indicates that the focal mechanism for these multiplets has a large uncertainty.

Table 2. Nodal planes strike, dip and rake and associated uncertainties (confidence level at 95 per cent) for the composite focal mechanisms computed in 1-D and 3-D velocity model.

Multiplet	Solution type	Plane 1						Plane 2					
		Plane parameters			Uncertainties			Plane parameters			Uncertainties		
		ϕf	δ	λ	$\Delta\phi f$	$\Delta\delta$	$\Delta\lambda$	ϕf	δ	λ	$\Delta\phi f$	$\Delta\delta$	$\Delta\lambda$
19	1-D	85	43	−74	8	3	8	244	49	−104	12	5	6
	3-D	125	57	−91	14	10	10	308	33	−88	28	11	12
573	1-D	80	31	−167	48	40	60	338	83	−59	70	40	44
	3-D	86	28	−168	62	41	52	345	84	−63	50	40	42
630	1-D	84	64	−131	8	12	20	327	47	−37	26	9	28
	3-D	90	51	−112	14	14	24	303	44	−65	26	7	34
724	1-D	46	87	−135	86	32	78	312	45	−5	72	29	44
	3-D	82	60	−97	40	16	40	276	31	−78	60	28	76
853	1-D	95	68	−107	6	8	6	314	27	−54	22	7	16
	3-D	94	63	−110	8	5	8	313	33	−56	20	5	10
866	1-D	190	41	−75	56	20	26	350	51	−103	36	20	48
	3-D	86	68	−116	66	21	20	318	34	−43	88	12	32
891	1-D	105	56	−90	26	10	20	284	34	−91	20	8	34
	3-D	122	64	−83	20	8	22	286	27	−105	22	12	34
1767	1-D	119	43	117	16	14	16	264	53	67	10	12	16
	3-D	115	36	112	42	20	52	268	57	75	28	20	54
2423	1-D	105	48	−78	8	5	14	268	43	−103	12	8	10
	3-D	101	44	−72	4	4	10	256	49	−107	10	6	8
2877	1-D	116	66	−83	50	6	20	279	24	−105	78	35	26
	3-D	116	66	−88	68	18	30	292	24	−94	34	23	34
3061	1-D	113	71	−78	54	6	26	261	22	−120	46	21	32
	3-D	104	77	−84	18	6	10	260	14	−114	24	8	30
3715	1-D	43	55	−76	16	10	30	200	37	−109	40	8	46
	3-D	47	57	−78	18	11	34	206	35	−108	38	10	46
3803	1-D	113	61	−77	12	9	12	268	31	−112	16	6	24
	3-D	116	55	−89	18	7	20	295	35	−91	18	8	28
3911	1-D	146	78	−15	88	25	6	239	75	−168	44	18	16
	3-D	87	33	−98	86	27	64	277	57	−85	30	15	54
3917	1-D	61	84	−169	44	29	42	330	79	−6	24	17	46
	3-D	111	28	−102	34	30	48	304	63	−84	24	12	20
4049	1-D	102	56	−69	10	7	20	247	40	−118	20	10	24
	3-D	99	55	−71	10	8	22	249	39	−115	24	12	18
4416	1-D	79	41	−108	38	23	48	283	51	−75	24	13	42
	3-D	86	38	−107	36	28	58	287	54	−77	34	13	48
4432	1-D	139	63	−33	34	20	42	246	61	−149	20	10	46
	3-D	85	39	−100	32	23	50	278	51	−82	32	14	42
4493	1-D	142	65	−33	34	24	46	247	60	−151	24	13	42
	3-D	89	40	−102	34	30	52	285	51	−80	36	13	46
4572	1-D	127	47	−48	14	17	22	254	57	−125	12	9	28
	3-D	123	45	−55	34	12	42	258	55	−120	22	8	34
4693	1-D	144	64	−9	42	32	42	238	82	−154	24	11	36
	3-D	94	18	−106	38	19	32	290	73	−85	8	8	8
4761	1-D	141	64	−46	34	31	10	255	50	−145	50	17	14
	3-D	142	62	−50	26	17	24	262	48	−140	14	9	32
5278	1-D	81	55	−130	6	9	10	316	51	−48	46	20	40
	3-D	86	56	−129	2	11	6	322	50	−47	44	21	30
18445	1-D	36	43	−98	72	13	42	227	48	−82	50	17	26
	3-D	95	34	−134	64	11	36	324	66	−65	34	12	22

The distribution of uncertainties on strike, dip and rake of the two nodal planes deduced from the perturbed solutions for the 24 multiplets are displayed in Fig. 5. The uncertainty range is similar for the 1-D and 3-D solutions. In overall, the use of the 3-D velocity model does not reduce the uncertainties (the median of the strike and rake uncertainty is even larger for the 3-D than for the 1-D solutions).

However, some clues lead us to be more confident in the 3-D solutions. First, the score function of the 3-D solutions is usually larger than the score of the 1-D solutions (Fig. 6) except for multiplets 01767, 02423 and 03715. But for these three multiplets the difference between the 1-D and 3-D score functions is very small. This indicates that the difference between the observed and theoretical amplitude ratios is globally reduced if the take-off angle and azimuth of the rays at the source are computed in the 3-D velocity model.

Second, the 24 3-D fault plane solutions are more homogeneous than the 1-D solutions and are more consistent with the tectonic setting. The representation in a ternary diagram (Kagan 2005) of the 1-D focal mechanisms (black points, Fig. 7a) shows they are

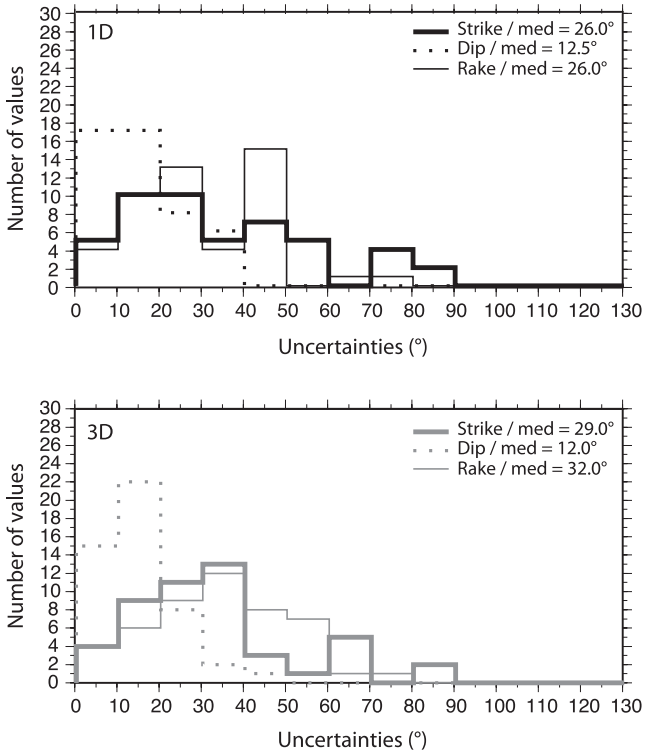

Figure 5. Histograms of the strike, dip and rake uncertainties (confidence level at 95 per cent) for the two nodal planes of the focal mechanisms computed in the 1-D (top panel) and 3-D (bottom panel) velocity model.

characterized by normal to strike-slip faults. Their nodal planes trend along one main direction (N240 and N270) and several other minor directions (Fig. 7b). *T* axes are scattered with a main sub-horizontal family along NNE–SSW direction and *P* axes are sub-horizontal to subvertical along ESE–WNW direction (Fig. 7c). 3-D solutions (red points) are essentially normal faults (Fig. 7a). The nodal planes (Fig. 7b) are distributed in two main families (E–NE/W–SW and W–NW/E–SE directions). *T* axes are mainly sub-horizontal along the NNE–SSW direction and *P* axes are subvertical (Fig. 7c). These results are in agreement with the NNE–SSW extensional/vertical shortening regional context.

Based on these observations, we will only consider the 3-D focal mechanisms in the following. The 24 multiplets with their 3-D fault plane solutions are plotted in map view and cross-section in Figs 8 and 9. There is focal solutions homogeneity for the multiplets located under the Gulf (NW–SE normal fault). On the other hand, the multiplets located under the northeastern coast display variability in the fault plane solutions.

4 FOCAL MECHANISMS AND MULTIPLETS ANALYSIS

The fault plane solutions are compared with the geometry of the multiplets. The geometry is determined using the three-point method (Fehler *et al.* 1987). The general principle is to take all possible combinations of three events in a multiplet and calculate the strike and dip of the plane defined by each combination. The pole density of the obtained planes is plotted for each multiplet on a stereogram with the pole of the nodal planes (Fig. 10).

For four multiplets (00630, 00891, 03061 and 03803; group A), the comparison between the geometry and the focal mechanism cannot be performed because the geometry from the three-point analysis is undefined (Fig. 10a). Multiplet 02423 (group B) has a clear geometry significantly different from the focal mechanism (Fig. 10b). Four multiplets (03917, 04416, 04432 and 18445; group C)) have a geometry unconstrained in dip (Fig. 10c). Thus, the two nodal planes are included in the uncertainty domain of the multiplet geometry. In these cases, inferring that the multiplet plane is a fault plane, it is not possible to determine which nodal plane is the fault plane. For the other 15 multiplets (group D; Fig. 10d), one of the nodal planes is very near to or falls in the uncertainty domain of the multiplet geometry. Therefore it is possible to determine which nodal plane is the fault plane. All the fault planes are dipping north except for multiplets 00019 and 01767 displaying southern dip.

The multiplets with northern steep dipping planes are located at the base of several major faults (Figs 8 and 9): the Aigion Fault, the Fassouleika Fault, the Selianitika Fault and two offshore faults. The dip of the Aigion Fault has been measured to be 60° in the first kilometre (Cornet *et al.* 2004) and we assume a 60° dip in the first kilometres depth for the other faults (Bernard *et al.* 2006). The fault plane solutions of the multiplets display a global E–W to NW–SE trend consistent with the azimuth of the major faults in the area. Steep dipping multiplets 04761 and 04572 are located in the downward continuation of the Fassouleika and Selianitika faults, which could take root on a low dipping structure (20°–30°)

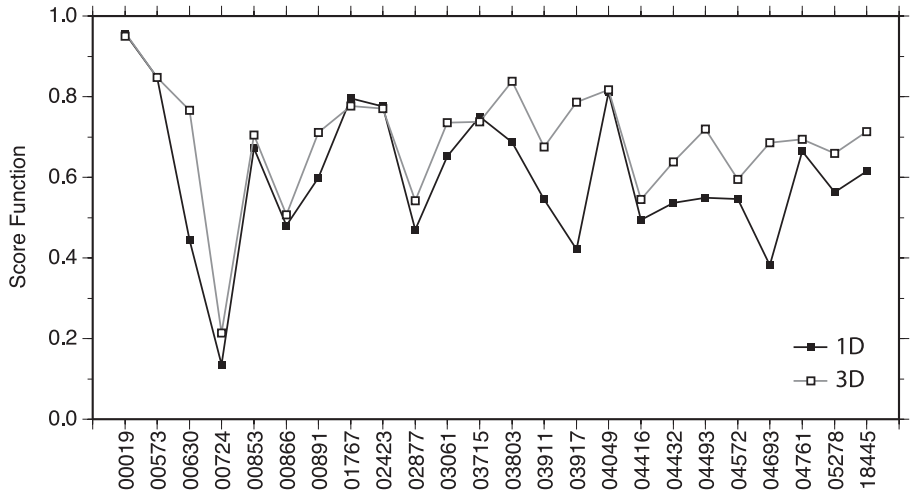

Figure 6. Score of the optimal fault plane solution for each multiplet computed in the 1-D velocity model (black) and the 3-D velocity model (white).

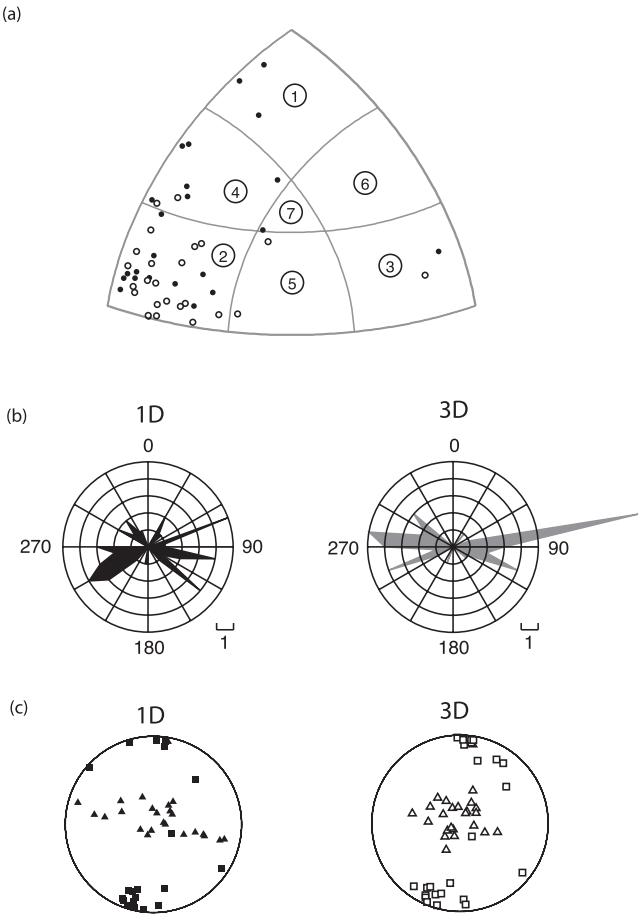

Figure 7. Composite fault plane solutions for 24 multiplets in the western part of the Corinth Rift. (a) Ternary diagram (Kagan 2005) displaying the solutions obtained using 1-D velocity model (black dot) and 3-D velocity model (white dot). The coordinates of each point in the ternary diagram are obtained from the plunge angle of the *P*-, *T*- and null axes. Each corner of the triangle corresponds to the vertical null-axis (strike-slip fault), *P*-axis (normal fault) and *T*-axis (thrust fault). The lines inside the diagram indicate the 30° plunge angle of the null-, *P*- and *T* axis and delineate seven areas corresponding to a type of focal mechanism: strike-slip fault (Area 1), normal fault (Area 2), inverse fault (Area 3), normal-strike-slip fault (Area 4), dip-slip fault (Area 5), thrust-strike-slip fault (Area 6) and mixed fault (Area 7). (b) Rose diagrams displaying the nodal planes azimuth of the focal mechanisms computed in the 1-D velocity model (left-hand side) and the 3-D velocity model (right-hand side). (c) *P* (triangle) and *T* (square) axis of the focal mechanisms computed in the 1-D velocity model (left-hand side) and the 3-D velocity model (right-hand side).

underlined by multiplets 00853, 02877, 03061 and 03803 (Fig. 9a). Multiplet 18445 is also characterized by a steep north dipping nodal plane but cannot be related to any known fault. On cross-section b–b′ (Fig. 9b) multiplets 03911, 03917 and 04693 highlight a steep north dipping structure in the continuation of the Aigion and Fassouleika faults. Multiplets 04416, 04432, 04493 and 05278 underline a steep north dipping structure that could correspond to the root of the Fassouleika or southern offshore fault on the eastern extent of the low dipping structure (∼30°) underlined by the multiplet 00724. Multiplet 00019 underlines an antithetic ESE–WNW south dipping structure (≈60°) potentially in the continuation of the Kalithea Fault. As a conclusion, it is noteworthy that even if some multiplets seem to be in continuity with the faults seen at the surface, there is no clear connection like seismicity linking surface and deep structures.

The multiplets on cross-section c–c′ (Fig. 9c) are located near the inferred rupture plane of the 1995 earthquake (Bernard *et al.* 1997). Multiplets 00630, 00891 and 00866 are on the western border of this rupture plane. Multiplet 0866 coincides with it (same depth and dip) whereas the two other multiplets are shifted in depth. Multiplet 04049 highlights a low north dipping structures (≈30°) under the northern coast in the continuity of the 1995 earthquake rupture plane.

The four multiplets on the cross-section d–d′ (Fig. 9d) are located in the continuation of the rupture plane of the 1995 earthquake. The fault plane solutions are different for each multiplet. These differences can be explained by the location of the multiplet in a transition zone (between an important seismic activity to the West and a very low seismic activity to the East) where the stress field might be heterogeneous. The multiplets are located on the northeastern borders of the seismological network and of the 3-D velocity model, which can also explain the differences in the fault plane solutions. Nevertheless, the focal solutions are in accordance with the multiplet geometry except for multiplet 02423. Multiplet 01767 is an E–W south dipping structure (≈30°) with an inverse focal mechanism. Such solution can be surprising in the overall extensional context of the Corinth Rift but it could be possible that a part of the extensional deformation along the low northern dipping structures is accommodated by minor inverse structures with southern dip.

Globally, cross-sections in Figs 9(a) and (b) show that southern normal-faulting active structures (in continuity with fault mapped at the surface) have steep dip whereas northern ones have shallow dip. This trend is clearly visible in Fig. 11 where the dip of the nodal planes dipping to the north (azimuth greater than 180°) is plotted versus the latitude and depth. We observe a decrease of the fault dip (from 70° to 15°) from south to north (Fig. 11a) and along the depth together (Fig. 11c). To the east (Figs 9c and d), the seismicity also reveals some shallow north dipping normal faults; but contrary to the western part, the dip decrease as a function of latitude and depth is not observed (Figs 11b and d).

In summary our results show (1) the southern active structures with steep dip are possibly the root of the Aigion, Fassouleika and Selianitika faults and (2) they might connect to a low angle structure dipping to the north.

5 DISCUSSION

For most of the studied multiplets, the compatibility between the multiplet geometry and one of the nodal planes confirms the geometry of the active structures inferred by the multiplet analysis of Lambotte *et al.* (in preparation): (1) multiplets in the shallow part of the seismic layer have higher dip than the layer itself, (2) in the deeper part multiplets have dip similar to the one of the layer. The joint analysis of the multiplet geometry and fault plane solution thus provides a high-resolution image of the active structures beneath the Corinth Rift.

Our results corroborate observations and interpretations of some previous studies. From a 2-month dense seismological experiment in 1991, Rigo *et al.* (1996) suggests the existence of an active north dipping low angle (15° ± 10°) detachment fault at about 10 km depth beneath the Gulf on which major faults seen at the surface appear to root. This hypothesis is reinforced by a fine analysis of a 12-earthquake cluster (master event relocation and focal mechanism determination) showing clear evidences for active low angle normal faulting (Rietbrock *et al.* 1996).

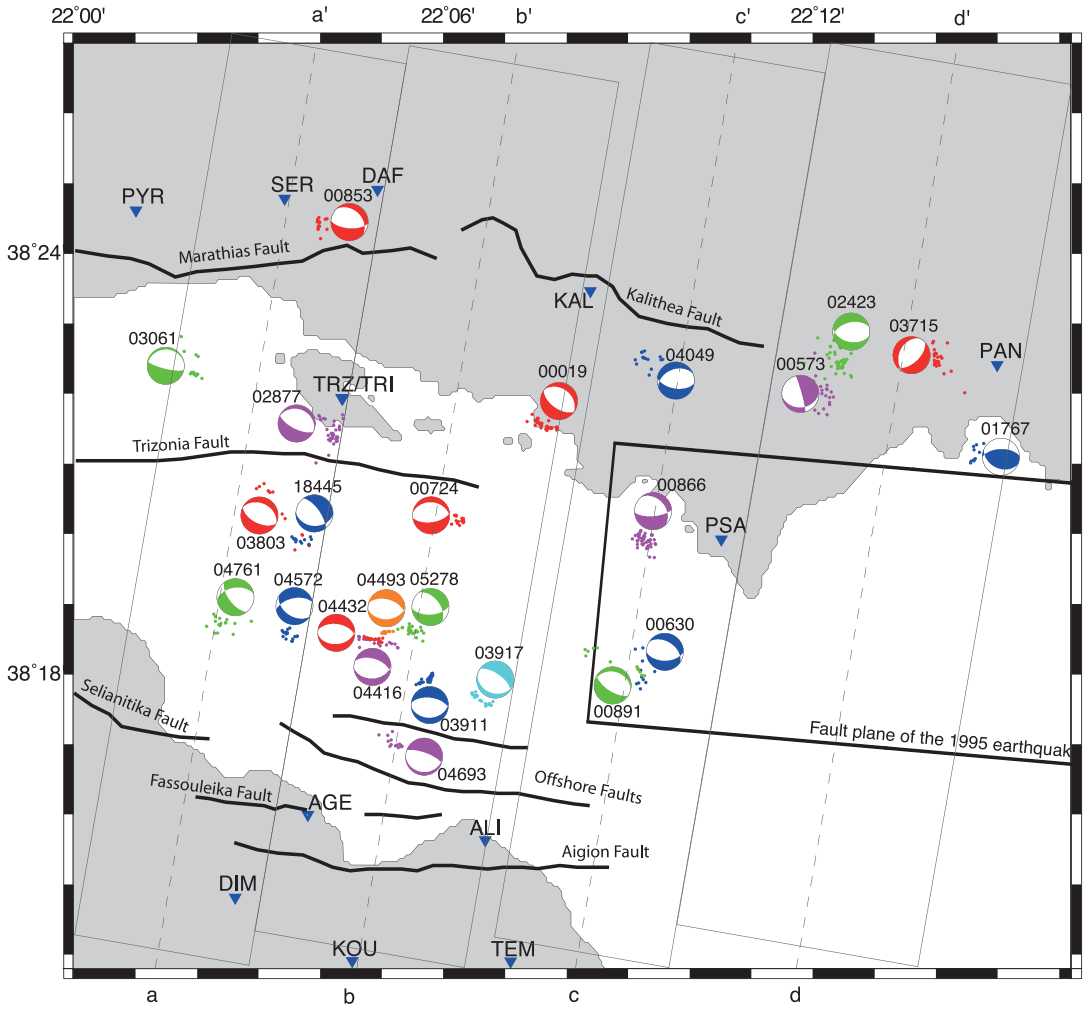

Figure 8. Map of the Western Corinth Rift displaying the 24 studied multiplets with the corresponding composite focal mechanisms, the main faults identified on the southern and northern coasts and the inferred rupture plane of the 1995 earthquake (Bernard *et al.* 1997).

Our results are also consistent with the mechanical model proposed by Lambotte *et al.* (in preparation). In this model, the opening of this part of the rift results from a non-elastic opening below the rift axis. The seismic layer represents a diffuse area of deformation which corresponds to an early stage of a detachment, growing downdip towards the north.

Our analysis highlights numerous normal-faulting active structures with low dip. Seismic activity on low angle normal fault has also been reported in the Woodlark Basin (Papua New Guinea, Abers *et al.* 1997) and Northern Apennines (Italy, Chiaraluce *et al.* 2007). From mechanical point of view, normal faulting on shallow dipping plane is a paradox and raises questions (e.g. Collettini 2011). Based on Coulomb's fracture criterion, normal faulting is impossible on low angle plane under normal conditions (σ1 vertical). Hence, special conditions as low friction coefficient or non-vertical σ1 are required. Rietbrock *et al.* (1996) postulate that the microseismicity is restricted to a zone of creep (low friction coefficient) but acknowledge that alternatively fluid pressures can play an important role by perturbing the stress field. Based on several field geological observations, Collettini (2011) proposes that (1) low angle normal faults act as preferential channel for fluid flow with, in some cases, fluid overpressure, (2) fluid–rock interaction can favour the development of phyllosilicates characterized by low friction coefficient and velocity-strengthening frictional behaviour (fault creeping). He therefore argues that such mechanical conditions can potentially promote normal-rupture on low angle faults.

Several evidences show that mechanical conditions for low angle normal faulting are potentially present in the western part of the Corinth Rift. Fluids have been recently evidenced by observations of earthquake migrations compatible with fluid diffusion process (Bourouis & Cornet 2009; Pacchiani & Lyon-Caen 2010). Moreover 3-D seismic tomography analysis (Latorre *et al.* 2004; Gautier *et al.* 2006) revealed high V_p/V_s anomalies at 8–12 km, which suggests a fluid saturated zone. Concerning fault creeping conditions, Latorre *et al.* (2004) argues that a sharp increase of seismic velocities at 5–7 km depth could represent the tectonic contact between the Gavrovo–Tripolitza tectonic unit and the Phyllite–Quartzite series (Xypolias & Koukouvelas 2001). Hence, the seismic layer would be located in phyllosilicate-rich rocks whose the frictional properties reduce the strength of faults.

6 CONCLUSION

The computation of composite focal mechanisms for 24 large earthquake multiplets and the joint analysis with the multiplet geometry have shown the influence of the velocity model and have provided constraints on the geometry of active faults in the Western part of the Corinth Rift.

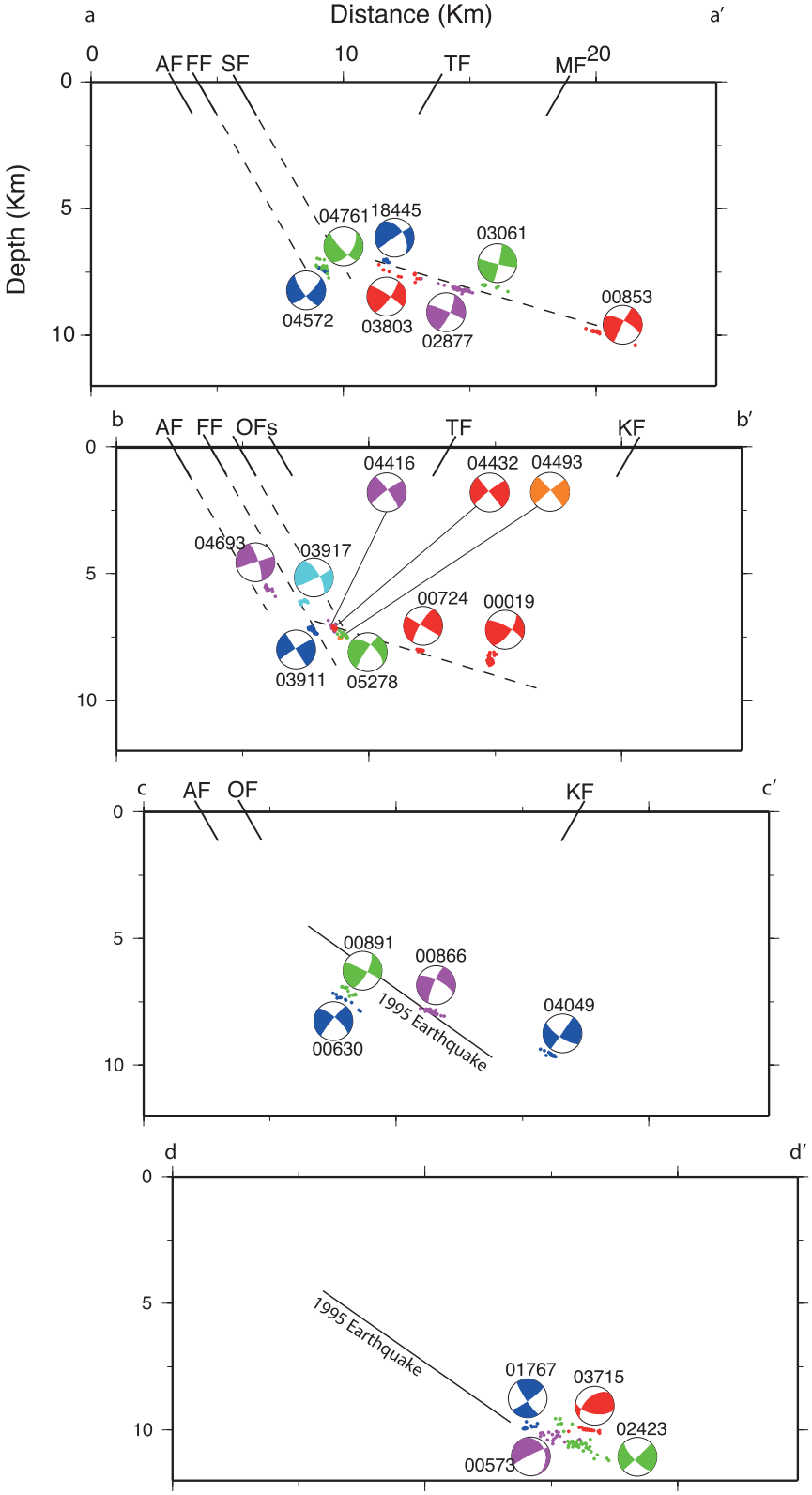

Figure 9. NE–SW cross-sections of the Western Corinth Gulf displaying the 24 studied multiplets with the corresponding composite focal mechanisms, the main faults identified on the southern and northern coasts and the inferred rupture plane of the 1995 earthquake. AF, Aigion Fault; FF, Fassouleika Fault; SF, Selianitika Fault; OFs, Offshore faults; TZ, Trizonia Fault; KF, Kalithea Fault; MF, Marathia Fault. For cross-section location see Fig. 8.

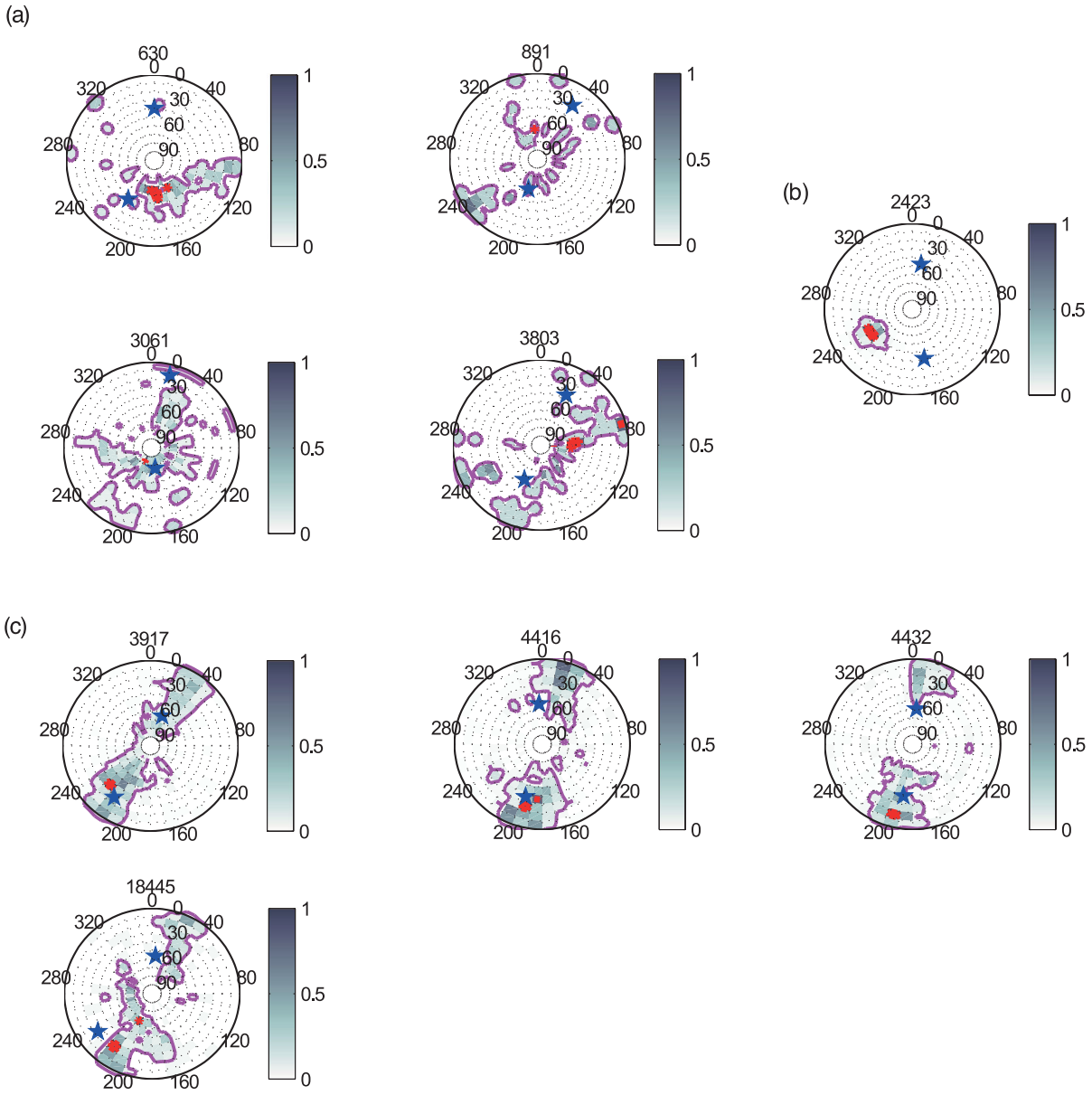

Figure 10. Comparison between the composite fault plane solutions and the geometry of the multiplets determined by the three-point method of Fehler *et al.* (1987). The stereograms are divided in a grid of 10° step in azimuth and dip. The grey scale indicates the pole density of planes defined by all combinations of three events in multiplets. The density is normalized by the maximum density of each stereogram. The contour lines delineate areas with normalized density, respectively, greater or equal than 0.8 (red) and 0.05 (purple). Blue stars indicate the poles of the nodal planes. (a) Multiplet with unconstrained geometry. (b) Multiplet with significant difference between the nodal planes and the geometry. (c) Multiplet with accordance between the two nodal planes and the geometry. (d) Multiplet with accordance between one of the nodal planes and the geometry.

The more or less significant difference between focal mechanisms from 1-D and 3-D velocity model indicates how the resolution of focal solutions is sensitive to vertical and azimuthal velocity variations. The use of a 3-D velocity model does not reduce uncertainties on the focal mechanisms. However, the better score function, the greater homogeneity in the focal solutions (normal faulting) and their better compatibility with the NNE–SSW extensional/vertical shortening tectonic context of the Corinth Rift indicate a better accuracy in the 3-D solutions.

The comparison between focal mechanism and multiplet geometry has shown that 15 multiplets have one of the nodal planes consistent with the plane delineated by the seismicity. This allows identifying which nodal plane is the fault plane. For the other seven multiplets, the geometry is unconstrained in strike and dip (no clear earthquakes alignment) or only unconstrained in dip. For this latter case, the two nodal planes are consistent with the multiplet geometry. Finally, only one multiplet displays geometry dramatically different from the focal mechanism (multiplet 02423). Consequently, multiplet geometry and focal mechanism are two complementary observations. The geometry of the multiplet allows determining which nodal plane is the fault plane. Inversely, focal mechanism indicates the rupture movement on the fault plane delineated by the multiplet.

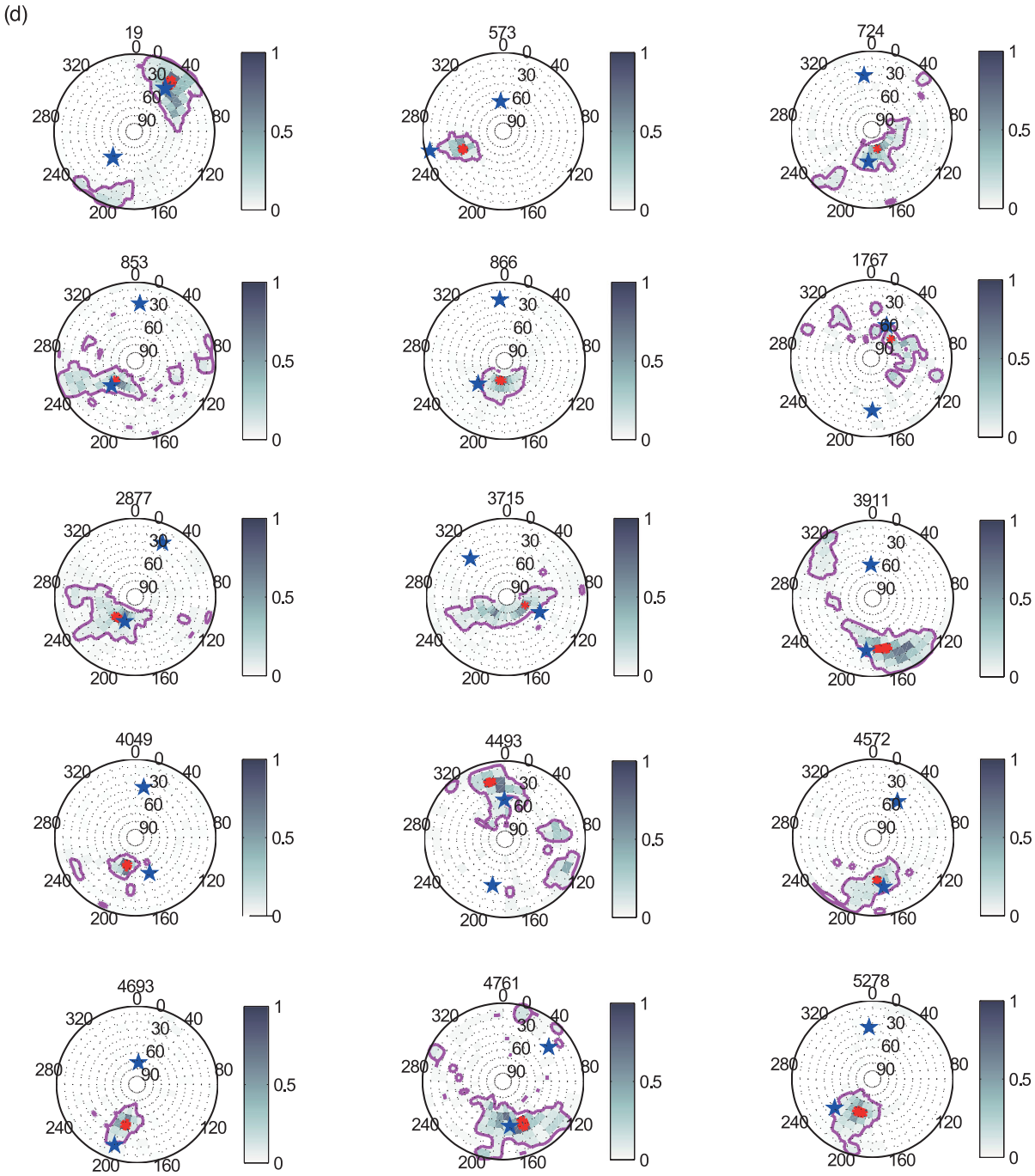

Figure 10. (*Continued.*)

The joint analysis of the multiplet geometry and focal mechanisms gives a high precision in the description of the active zones in the western part of the Corinth Rift. The extensional regime in the central part of the studied zone is confirmed. The geometry of the active structures inferred by the multiplet analysis of Lambotte *et al.* (in preparation) is corroborated.

Several multiplets seem to coincide at depth with the downward extension of the Aigion, Fassouleika, Selianitika and offshore faults implying that their dip (∼60°) stays more or less constant from the surface down to ∼7 km. A low, north dipping structure (20°–30°), on which steep north dipping faults seem to root, has been also highlighted under the Corinth Gulf and its northern coast.

These results reinforce the hypothesis of a north dipping low angle detachment zone beneath the northern part of the rift on which major faults seen at the surface seem to root (Rigo *et al.* 1996; Lambotte *et al.*, in preparation). However, such a model raises the mechanical problem of the existence of active low angle normal faults.

ACKNOWLEDGEMENTS

We gratefully acknowledge the two anonymous reviewers whose comments helped us to improve the manuscript. CRLNET has been

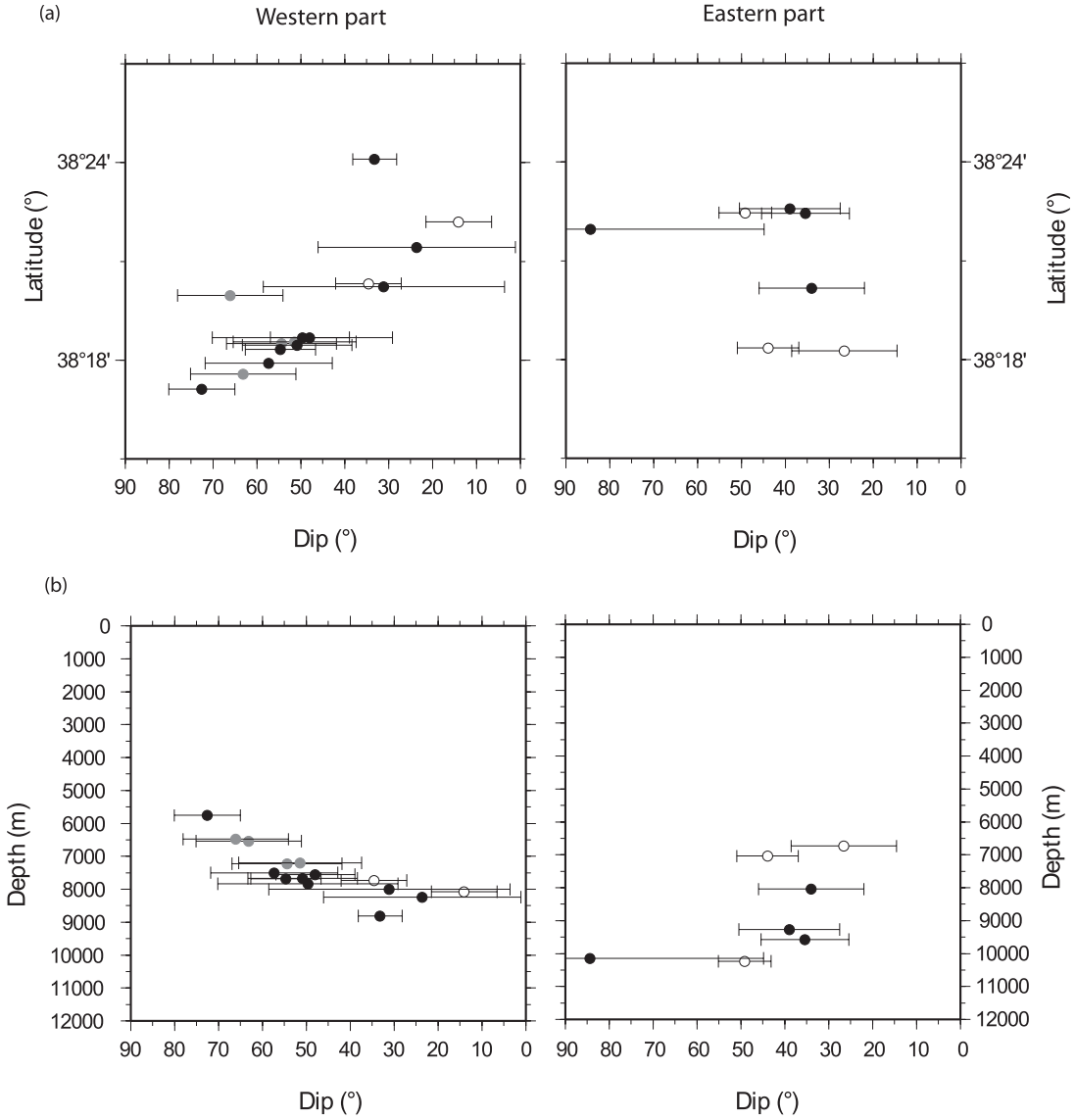

Figure 11. (a) Dip values of the nodal planes dipping to the north (azimuth greater than 180°) versus the latitude. (b) Dip values of the nodal planes dipping to the north versus depth. The multiplets with south dipping fault planes (00019 and 01767) are not represented. The black symbols are the nodal planes in accordance with the multiplets geometry, the grey symbols are the nodal planes of the multiplets with unconstrained dip geometry and the white symbols are the nodal planes different from the multiplets geometry and the multiplet with unconstrained geometry. Eastern part plot displays multiplets of the cross-sections a–a′ and b–b′ (Fig. 9). Western part plot displays multiplets of the cross-sections c–c′ and d–d′.

supported by INSU CNRS in France, by the European Community through the CORSEIS and 3HAZ projects and by Agence Nationale de la Recherche with the CatTel@crl and SISCOR projects.

REFERENCES

Abers, G., Mutter, C. & Fang, J., 1997. Shallow dips of normal faults during rapid extension: earthquakes in the Woodlark-d'Entrecasteaux rift system, Papua New Guinea, *J. geophys. Res.,* **102,** 15 301–15 317.

Aki, K. & Richards, P., 1980. *Quantitative Seismology: Theory and Methods,* Freeman & Co.

Ambraseys, N. & Jackson, J., 1990. Seismicity and associated strain of central Greece between 1890 and 1988, *Geophys. J. Int.,* **101,** 663–708.

Armijo, R., Meyer, B., King, G., Rigo, A. & Papanastassiou, D., 1996. Quaternary evolution of the Corinth rift and its implications for the Late Cenozoic evolution of the Aegean, *Geophys. J. Int.,* **126,** 11–53.

Avallone, A. *et al.*, 2004. Analysis of eleven years of deformation measured by GPS in the Corinth Rift Laboratory area, *C. R. Geoscience,* **336,** 301–311.

Bernard, P. *et al.*, 1997. The Ms = 6.2, June 15, 1995 Aigion earthquake (Greece): evidence for low angle normal faulting in the Corinth rift, *J. Seismol.,* **1,** 131–150.

Bernard, P. *et al.*, 2006. Seismicity, deformation and seismic hazard in the western rift of Corinth: new insights from the Corinth Rift Laboratory (CRL), *Tectonophysics,* **426,** 7–30.

Bourouis, S. & Cornet, F.H., 2009. Microseismic activity and fluid fault interactions: some results from the Corinth Rift Laboratory (CRL), Greece, *Geophy. J. Int.,* **178**(1), 561–580.

Briole, P., Deschamps, A., Lyon-Caen, H., Papazissi, K. & Martinod, J., 1993. The Itea (Ms = 5.9) earthquake of November 18, 1992: characteristics of the main shock inferred from body wave and ground displacement analysis, in *Proceedings of 2nd Hellenic Geophysical Union,* Florina, Greece.

Chiaraluce, L., Chiarabba, C., Collettini, C., Piccinini, D. & Coco, M., 2007. Architecture and mechanics of an active low-angle normal fault: Alto Tiberina fault, northern Apennines, Italy, *J. geophys. Res.,* **112,** B10310, doi:10.1029/2007JB005015.

Collettini, C., 2011. The mechanical paradox of low-angle normal faults: current understanding and open questions, *Tectonophysics,* **510,** 253–268.

Cornet, F., Doan, M., Moretti, I. & Borm, G., 2004. Drilling through the active Aigion fault: the AIG10 well observatory, *Comptes Rendus Geosci.,* **336,** 395–406.

Fehler, M., House, L. & Kaieda, H., 1987. Determining planes along which earthquakes occur: method and application to earthquakes accompanying hydraulic fracturing, *J. geophys. Res.,* **92,** 9407–9414.

Gautier, S., Latorre, D., Virieux, J., Deschamps, A., Skarpelos, C., Sotiriou, A., Serpetsidaki, A. & Tselentis, A., 2006. A new passive tomography of the Aigion area (Gulf of Corinth, Greece) from the 2002 data set, *Pure appl. Geophys.,* **163,** 431–453.

Gautier, S., Nolet, G. & Virieux, J., 2008. Finite-frequency tomography in a crustal environment: application to the western part of the Gulf of Corinth, *Geophys. Prospect.,* **56**(4), 493–503.

Godano, M., Regnier, M., Deschamps, A., Bardainne, T. & Gaucher, E., 2009. Focal mechanisms from sparse observations by nonlinear inversion of amplitudes: method and tests on synthetic and real data, *Bull. seism. Soc. Am.,* **99**(4), 2243–2264.

Hardebeck, J. & Shearer, P., 2003. Using S/P amplitude ratios to constrain focal mechanisms of small earthquakes, *Bull. seism. Soc. Am.,* **93**(6), 2434–2444.

Jechumtalova, Z. & Šileny, J., 2005. Amplitude ratios for complete moment tensor retrieval, *Geophys. Res. Lett.,* **32,** L22303, doi:10.1029/2005GL023967.

Julian, B., Miller, A. & Foulger, G., 1998. Non-double-couple earthquakes 1: theory, *Rev. Geophys.,* **36,** 525–549.

Kagan, Y., 2005. Double-couple earthquake focal mechanism: random rotation and display, *Geophys. J. Int.,* **163,** 1065–1072.

King, G. *et al.*, 1985. The evolution of the Gulf of Corinth (Greece): an aftershock study of the 1981 earthquakes, *Geophys. J. R. astr. Soc.,* **80,** 677–693.

Kirkpatrick, S., Gelatt, C. & Vecchi, M., 1983. Optimization by simulated annealing, *Science,* **220**(4598), 671–680.

Komatitsch, D., Liu, Q., Tromp, J., Süss, P., Stidham, C. & Shaw, J., 2004. Simulations of ground motion in the Los Angeles basin based upon the spectral-element method, *Bull. seism. Soc. Am.,* **94**(1), 187–206.

Latorre, D., Virieux, J., Monfret, T., Monteiller, V., Vanorio, T., Got, J.-L. & Lyon-Caen, H., 2004. A new seismic tomography of Aigion area (Gulf of Corinth, Greece) from the 1991 dataset, *Geophys. J. Int.,* **159,** 1013–1031.

Lomax, A., Virieux, J., Volant, P. & Berge, C., 2000. *Probabilistic Earthquake Location in 3D and Layered Models: Introduction of a Metropolis-Gibbs Method and Comparison with Linear Locations. In: Advances in Seismic Event Location,* Kluwer.

Lyon-Caen, H., Papadimitriou, P., Deschamps, A., Bernard, P., Makropoulos, K., Pacchiani, F. & Patau, G., 2004. First results of the CRLN seismic network in the western Corinth Rift: evidence for old-fault reactivation, *C. R. Geosci.,* **336,** 343–351.

Moretti, I., Sakellariou, D., Lykousis, V. & Micarelli, L., 2003. The Gulf of Corinth: an active half Graben?, *J. Geodyn.,* **36,** 323–340.

Pacchiani, F., 2006. *Etude sismologique des failles normales actives du rift de Corinthe, PhD thesis*, Universite Paris XI, Paris.

Pacchiani, F. & Lyon-Caen, H., 2010. Geometry and spatio-temporal evolution of the 2001 Agios Ioanis earthquake swarm (Corinth rift, Greece), *Geophys. J. Int.,* **180**(1), 59–72.

Palyvos, N., Pantosti, D., DeMartini, P.M., Sorel, D. & Pavlopoulos, K., 2005. Aigion Neos Erineos normal fault system (Western Corinth Gulf Rift, Greece): geomorphological signature, recent earthquake history and induced coastal changes during the Holocene, *J. geophys. Res.,* **110,** B09302, doi:10.1029/2004JB003165.

Papazachos, C.B., 1992. Anisotropic radiation modelling of macroseismic intensities for estimation of the attenuation structure of the upper crust in Greece, *Pure appl. Geophys.,* **138,** 445–469.

Papazachos, B. & Papazachou, C., 1997. *The Earthquakes of Greece,* P. Ziti and Co.

Podvin, P. & Lecomte, I., 1991. Finite difference computation of traveltimes in very contrasted velocity models: a massively parallel approach and its associated tools, *Geophys. J. Int.,* **105,** 271–284.

Rietbrock, A., Tiberi, C., Scherbaum, F. & Lyon-Caen, H., 1996. Seismic slip on low angle normal fault in the Gulf of Corinth: evidence from high resolution cluster analysis of microearthquakes, *Geophys. Res. Lett.,* **23,** 1817–1820.

Rigo, A., Lyon-Caen, H., Armijo, R., Deschamps, A., Hatzfeld, D., Makropoulos, K., Papadimitriou, P. & Kassaras, I., 1996. A microseismic study in the western part of the Gulf of Corinth (Greece): implications for large-scale normal faulting mechanisms, *Geophys. J. Int.,* **126,** 663–688.

Saenger, E., Gold, N. & Shapiro, S., 2000. Modeling the propagation of elastic waves using a modified finite-difference grid, *Wave Motion,* **31**(1), 77–92.

Snoke, J.A., Munsey, J.W., Teague, A.G. & Bollinger, G.A., 1984. A program for focal mechanism determination by combined use of polarity and SV-P amplitude ratio data, *Earthquake Notes,* **55**(3), 15.

Sokos, E. *et al.*, 2012. January 2010 Efpalio earthquake sequence in the western Corinth Gulf (Greece), *Tectonophysics,* **530–531,** 299–309.

Waldhauser, F. & Ellsworth, W., 2000. A double-difference earthquake location algorithm: method and application to the Northern Hayward fault, California, *Bull. seism. Soc. Am.,* **90**(6), 1353–1368.

Xypolias, P. & Koukouvelas, I., 2001. Kinematic vorticity and strain rate patterns associated with ductile extrusion in the Chelmos shear zone (External Hellenides, Greece), *Tectonophysics,* **338,** 59–77.

APPENDIX A

Table A1. Date, time, E–W, N–S, depth coordinates (from a reference point located at 21.6°E and 38°N), nodal planes strike, dip and rake for the representative focal mechanisms computed by Pacchiani (2006).

Date	Time	X (m)	Y (m)	Z (m)	Plane 1			Plane 2		
					ϕf	δ	λ	ϕf	δ	λ
2001–05–01	21:02:00.30	35507.9163	41829.5738	8190	237	70	171	330	82	20
2001–11–05	14:40:20.45	44983.153	37593.8177	6760	270	59	−70	55	36	−120
2001–01–21	02:00:42.72	45039.1752	32245.893	6900	0	44	80	194	47	100
2001–08–03	08:04:13.25	41431.0263	40015.9092	8520	93	76	−117	336	30	−30
2001–09–10	14:00:44.84	49530.5445	37176.5959	8450	74	75	−94	270	16	−75
2001–12–31	06:31:59.88	53111.6975	41537.9666	10090	145	71	−88	320	19	−95
2001–03–15	15:17:33.08	43705.4271	31439.6734	8220	50	37	−170	312	84	−53
2001–01–14	22:54:42.99	44602.3886	32154.7051	6450	110	49	−80	274	41	−101
2001–12–07	22:44:50.74	49462.8521	26801.4503	5810	80	65	−125	319	42	−39
2001–11–01	05:51:10.21	49742.3323	39685.6137	10240	32	65	144	139	58	30
2001–02–08	23:04:08.95	44860.14	32988.322	5000	115	41	−72	272	51	−105

APPENDIX B

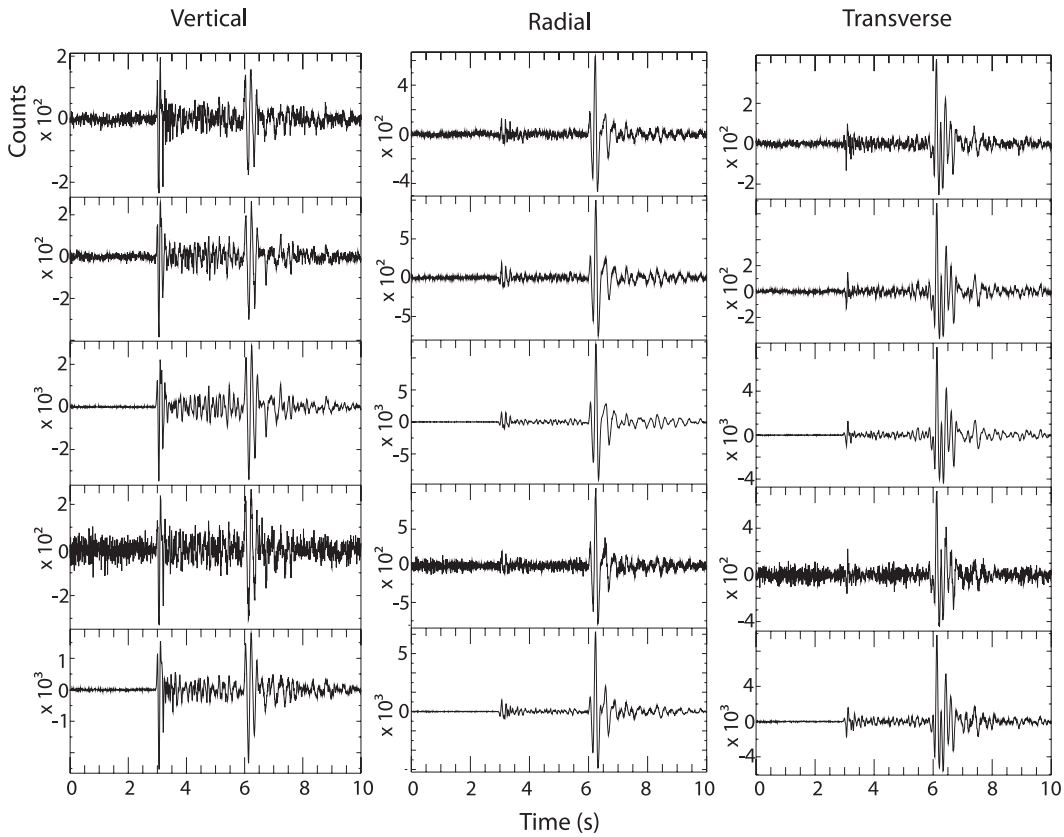

Figure B1. Waveforms recorded by the station PAN for the five earthquakes of the multiplet 04432 used for the focal mechanism computation.

APPENDIX C

Table C1. Date and time of the earthquakes used to compute the composite focal mechanism of each multiplet.

19	2423	4416
2000/07/08 18:09:49	2002/06/04 21:31:56	2004/02/24 17:30:47
2000/07/08 18:11:55	2003/11/16 19:07:45	2004/02/24 19:25:06
2000/07/08 19:19:49	2007/02/12 20:17:06	2004/02/26 19:09:36
2000/07/08 17:40:09		2004/02/26 23:25:16
2000/07/08 19:29:35		2004/02/27 06:58:31
		2004/03/31 10:26:17
573	2877	4432
2001/06/11 00:42:43	2002/09/22 04:50:40	2004/02/27 08:33:55
2001/07/09 13:20:47	2004/01/26 02:18:27	2004/01/29 01:25:34
	2004/03/31 14:16:24	2004/02/29 04:42:56
	2001/12/09 10:00:46	2004/02/29 07:37:27
	2002/02/27 22:50:54	2004/02/29 09:07:28
	2004/01/27 20:15:51	
630	3061	4493
2002/05/22 04:06:05	2004/08/24 03:15:20	2004/03/06 10:03:42
2002/02/09 14:42:24	2006/12/26 08:18:13	2002/11/10 12:01:02
		2007/01/25 14:00:59
724	3715	4572
2001/06/21 00:48:56	2002/12/28 19:42:26	2004/03/11 08:25:37
2002/05/14 19:12:17	2003/11/08 21:05:05	2004/03/16 20:34:26
2003/03/11 02:09:07	2004/11/19 20:37:10	2004/03/17 18:25:02
2003/08/08 04:18:10	2004/11/24 05:39:39	2004/03/17 18:50:16
853	3803	4693
2002/05/20 20:50:21	2004/07/26 11:08:26	2004/03/24 15:31:34
2004/12/31 04:37:29	2002/01/25 20:19:43	2002/06/22 06:30:48
2005/06/11 14:47:08	2002/06/13 20:09:02	2002/11/24 06:06:27
2006/10/30 01:20:39		2005/10/25 23:24:16
866	3911	4761
2002/01/04 13:48:28	2004/01/18 21:13:18	2004/04/12 03:37:33
2003/02/18 10:36:21	2004/01/22 23:33:46	2004/04/12 03:46:44
2003/07/19 10:17:16	2004/01/23 02:21:53	2004/04/12 05:14:45
2006/12/26 06:37:43	2004/01/23 12:47:52	2004/04/12 17:20:57
2007/06/21 03:58:27		
891	3917	5278
2001/08/03 22:32:10	2003/12/27 14:00:58	2007/01/11 23:30:03
2003/03/08 04:20:03	2004/01/17 01:49:24	2007/02/02 20:00:37
2007/04/04 21:50:30	2004/01/17 02:02:22	2007/02/03 17:00:08
	2004/01/18 05:35:47	2007/02/03 18:51:48
	2004/03/09 09:34:40	2007/02/03 21:35:20
1767	4049	18445
2001/11/02 12:57:04	2002/10/29 01:37:43	2007/03/20 18:21:01
2001/11/13 02:22:40	2003/03/16 14:32:58	2007/03/21 06:04:11
2005/12/01 03:44:14	2006/08/10 00:21:37	2007/05/27 09:29:56
2007/04/12 13:31:24		
2006/04/04 22:52:08		

APPENDIX D

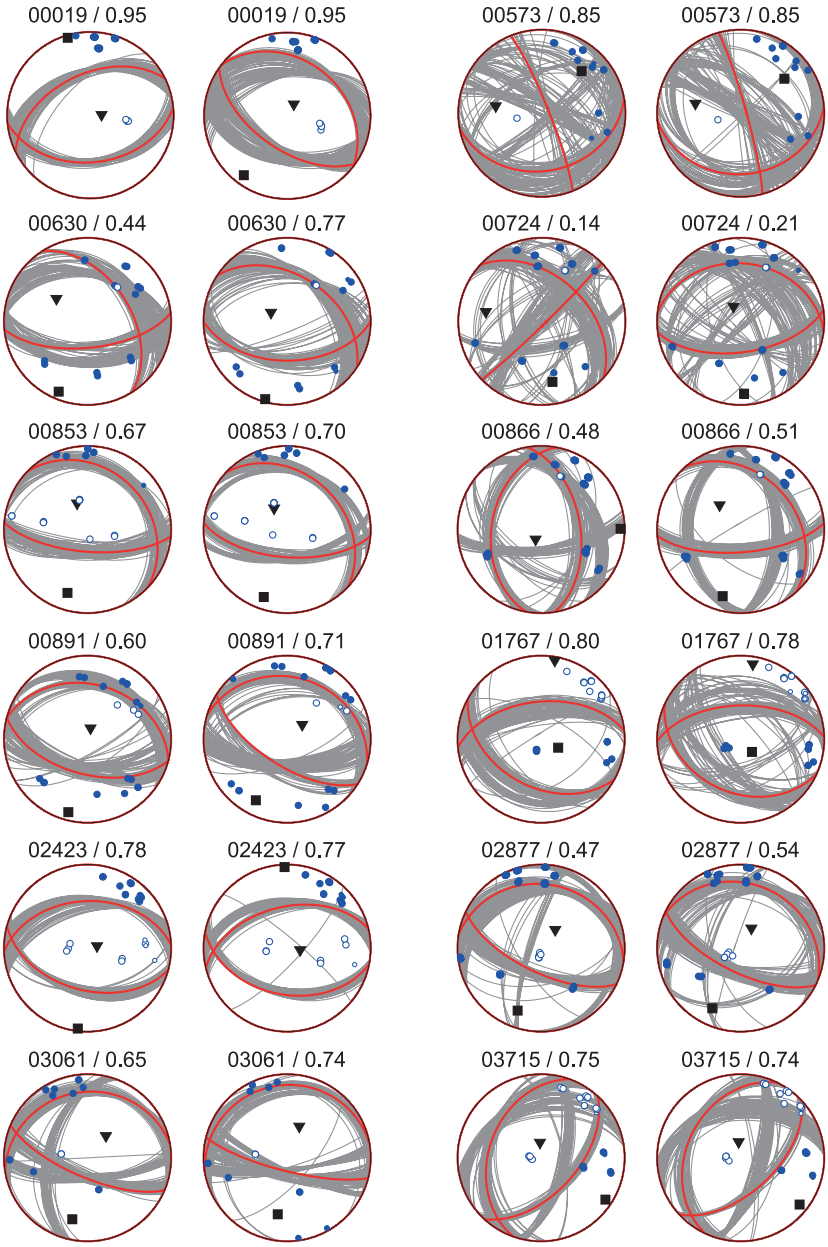

Figure D1. Optimal composite fault plane solutions of the 24 studied multiplets computed in a 1-D velocity model and a 3-D velocity model (red line) and the associated perturbed solutions used to compute the uncertainties (grey lines). The *P* (black triangle) and *T* (black square), *P*-wave compressions (blue circles) and dilatations (white circles) are plotted on each stereogram. The numbers above the stereograms are the multiplet name (left-hand side) and the score function of the optimal fault plane solution (right-hand side).

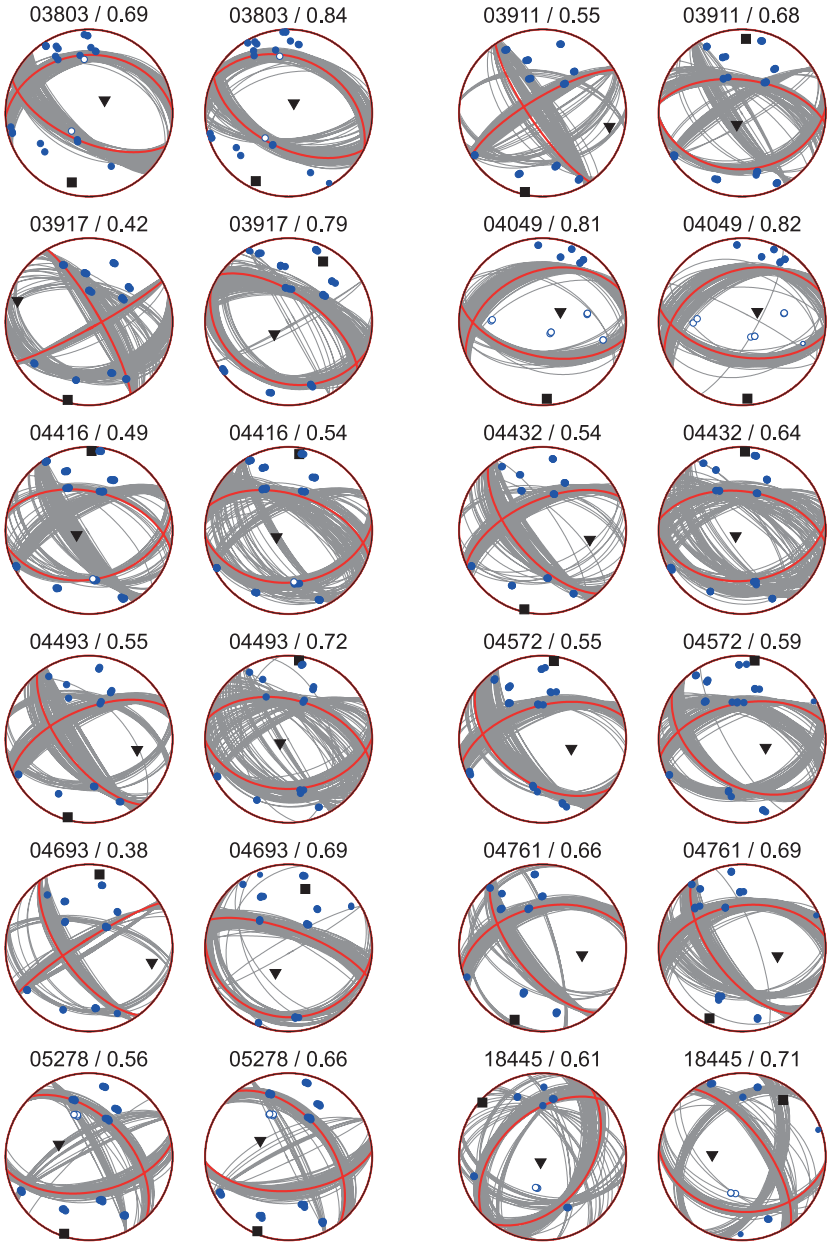

Figure D1. (*Continued.*)